Astrocytic RNA editing regulates the host immune response to alpha-synuclein

Karishma D'Sa[*1,2,3], Minee L. Choi[*1,2,3,4], Aaron Z. Wagen[*1,2,3,5], Núria Setó-Salvia[1,6], Olga Kopach[7,8], James R. Evans[1,2,3], Margarida Rodrigues[9,10], Patricia Lopez-Garcia[1,2,3], Joanne Lachica[1,2,3,11], Benjamin E. Clarke[2,12], Jaijeet Singh[1,2], Ali Ghareeb[1,13], James Bayne[13,14], Melissa Grant-Peters[3,5], Sonia Garcia-Ruiz[3,5], Zhongbo Chen[1,2], Samuel Rodriques[13,15], Dilan Athauda[1,2], Emil K. Gustavsson[3,5,11], Sarah A. Gagliano Taliun[16,17], Christina Toomey[1,2,3,11], Regina H. Reynolds[3,5], George Young[2,18], Stephanie Strohbuecker[2,3], Tom Warner[1,6], Dmitri A. Rusakov[7], Rickie Patani[2,12], Clare Bryant[19], David A. Klenerman[9,10], Sonia Gandhi[1,2,3*†], Mina Ryten [3,5,10,20,21*†]

[1]Department of Clinical and Movement Neurosciences, UCL Queen Square Institute of Neurology, Queen Square, London, UK

[2]The Francis Crick Institute, 1 Midland Road, London, UK

[3]Aligning Science Across Parkinson's (ASAP) Collaborative Research Network, Chevy Chase, MD, 20815

[4]Department of Brain & Cognitive Sciences, KAIST, 921 Dehak-ro, Daejeon, Republic of Korea

[5]Department of Genetics and Genomic Medicine, Great Ormond Street Institute of Child Health, University College London, London, UK

[6]Reta Lila Weston Institute, UCL Queen Square Institute of Neurology, London, UK

[7]Department of Clinical and Experimental Epilepsy, UCL Queen Square Institute of Neurology, London, WC1N 3BG UK

[8]Neuroscience & Cell Biology Research Institute, City St George's, University of London, Cranmer Terrace, London, SW17 0RE, UK

[9]Department of Chemistry, University of Cambridge, Cambridge, UK.

[10]UK Dementia Research Institute at The University of Cambridge, Cambridge, United Kingdom.

[11]UCL Queen Square Institute of Neurology, University College London, London, UK

[12]Department of Neuromuscular Disease, UCL Queen Square Institute of Neurology, Queen Square, London, WC1N 3BG UK

[13]Applied Biotechnology Lab, The Francis Crick Institute.

[14]Nuffield Department of Orthopaedics, Rheumatology and Musculoskeletal Sciences, University of Oxford, Oxford UK

[15]FutureHouse, 1405 Minnesota Street, San Francisco, CA, 94107, USA

[16]Montréal Heart Institute, Montréal, QC, Canada

[17]Department of Medicine & Department of Neurosciences, Université de Montréal, Montréal, QC, Canada.

[18]MRC Laboratory of Medical Sciences, London

[19]Department of Veterinary Medicine, University of Cambridge, Cambridge CB3 0ES, UK

[20]Department of Clinical Neurosciences, School of Clinical Medicine, The University of Cambridge, Cambridge, UK

[21]Department of Genetics, University of Cambridge, Cambridge, UK

[*] Joint Authors

[†] Corresponding Authors

Licence : CC-BY 4.0

Abstract

RNA editing is a post transcriptional mechanism that targets changes in RNA transcripts to modulate innate immune responses. We report the role of astrocyte specific, ADAR1 mediated RNA editing in neuroinflammation in Parkinson's disease. We generated hiPSC-derived astrocytes, neurons and co-cultures and exposed them to small soluble alpha-synuclein aggregates. Oligomeric alpha-synuclein triggered an inflammatory glial state associated with TLR activation, viral responses, and cytokine secretion. This reactive state resulted in loss of neurosupportive functions, and the induction of neuronal toxicity. Notably, interferon response pathways were activated leading to upregulation, and isoform switching of the RNA deaminase enzyme, ADAR1. ADAR1 mediates A-to-I RNA editing, and increases in RNA editing were observed in inflammatory pathways in cells, as well as in post-mortem human PD brain. Aberrant, or dysregulated, ADAR1 responses and RNA editing may lead to sustained inflammatory reactive states in astrocytes triggered by alpha-synuclein aggregation, and this may drive the neuroinflammatory cascade in Parkinson's.

Introduction

Parkinson's disease (PD) is a progressive neurodegenerative condition characterised by the accumulation of intraneuronal aggregates of alpha-synuclein (α-syn) through the brain(*1*). Astrogliosis has been reported in post-mortem Parkinson's brain(*2–7*), and in rodent models of synucleinopathy,[8,9] and astrocytes accumulate α-syn inclusions(*10*), raising a role for astrocytes, and astrocyte-mediated immune cascades(*11*), in triggering or driving PD pathogenesis. Astrocytes are an abundant glial cell, essential for neuronal function, and survival through the maintenance of CNS homeostasis via modulation of neurotransmitters and synapse formation, ionic balance, and maintenance of the blood-brain barrier(*12*). Reactive astrogliosis defines a process whereby, in response to pathology, astrocytes undergo changes in transcriptional regulation, biochemical, morphological, metabolic, and physiological remodeling, which ultimately result in a switch from resting to reactive states. The nature of the underlying stimulus (neuroinflammatory vs ischaemic) has defined certain reactive astrocyte states into neurotoxic (so called A1, which promote lipid mediated

77 neuronal death via activated microglia) and neuroprotective (so called A2, which promote
78 neuronal survival and regeneration through neurotrophic factors)(*13*). Reactive
79 transformation can be associated with loss of neurosupportive and homeostatic functions,
80 reduced synapse formation(*14*), alterations in glutamate uptake and recycling(*15*), and
81 dysregulated calcium signalling(*16*). Simultaneously reactive states are associated with the
82 gain of neurotoxic properties(*17*).

83

84 Focusing on PD, there is evidence that A1 astrocytes have been shown to infiltrate brain
85 regions associated with PD, including the striatum(*13*). Astrocytes in these regions express
86 the highest regional levels of immune mediators, such as toll-like receptor 4 (TLR4) and
87 myeloid differentiation primary response 88 (MyD88) , correlating with PD pathology(*18*).
88 Significantly, inhibiting the formation of these A1 astrocytes by blocking microglia-astrocytic
89 cross talk is neuroprotective in mouse models of PD(*19*). Reactive astrocyte substates are
90 likely to be diverse beyond these two states(*14*, *20*), and involve several exogenous and
91 endogenous triggers such as damage-associated molecular patterns (DAMPs) or proteostatic
92 stresses induced by misfolded proteins. Compared to control cell lines, human astrocytic
93 models of PD release increased amounts of pro-inflammatory cytokines in response to α-
94 syn(*21*). Moreover, in response to α-syn fibrils, iPSC-derived astrocytes can assume an antigen
95 presenting function, with upregulation of major histocompatibility complex (MHC) genes and
96 relocation of HLA molecules to the cell surface to present α-syn fibril peptides to neighbouring
97 cells(*21*). This finding, replicated in post-mortem brain samples(*22*), supports the idea that
98 astrocytes may mediate the immune response in the brain.

99 We have recently reported that physiological concentrations of oligomeric α-syn, trigger a
100 TLR4-dependent inflammatory response in murine primary astrocytes(*18*). The small soluble
101 hydrophobic and beta sheet rich aggregates, or oligomers of α-syn are known to be
102 neurotoxic, and trigger cell selective processes that are specific to the structural conformation
103 of the protein(*23–26*).

104 Sub-state modelling has been achieved in human iPSC-derived astrocytes and co-cultures(*27*),
105 which enable capture at a molecular level of cell autonomous and non-cell autonomous
106 cascades in pathology. We investigate how human iPSC-derived astrocytes respond to α-syn
107 oligomers (αsyn-O), which downstream response pathways are activated, and how this

108 reactivity affects neurons. We integrate bulk and single-cell transcriptomic, functional and
109 biophysical approaches in five lines of human iPSC-derived (hiPSC-derived) astrocytes (3 in-
110 house and 2 commercial lines), both alone and in co-culture with neurons, to define the
111 molecular response of astrocytes to misfolded α-syn. Finally, identifying innate immune
112 pathways of interest, we explore those pathways in post-mortem brain samples from those
113 with PD.

114 Results

115 Generation and functional characterisation of hiPSC-derived astrocytes and neurons alone
116 or in co-culture

117 We generated hiPSC-derived astrocytes from 5 healthy donors, and cortical neurons from a
118 sixth healthy donor (**Supp table 1**)(*28*). We compared the cellular response to αsyn-O in
119 astrocyte only, neuron only and astro-neuronal cultures (**Figure 1a**). Highly enriched cultures
120 of cortical astrocytes in feeder-free conditions were generated from three in-house lines
121 using an optimised small molecule serum free protocol, and two were purchased
122 commercially, derived through a proprietary serum free protocol (**Figure 1b**). We used the Shi
123 et al., 2012 protocol (**Figure 1b**) to generate highly enriched (>90%) and functional hiPSC-
124 derived cortical neurons from neural precursor cells(*24*, *25*).

125 Immunolabelling with GFAP, an astrocyte-specific marker demonstrated that cultures
126 contained >90% mature astrocytes (**Figure 1c**). hiPSC-derived astrocytes also displayed
127 cytosolic calcium responses on application of ATP as assessed using Fura-2 (**Figure 1d, e**)(*29*).
128 All lines demonstrated appropriate Na+ dependent uptake of glutamate from the
129 extracellular space, one of the major astrocytic functions that indicates functional activity of
130 Excitatory Amino Acid Transporter 1/2 in hiPSC-derived astrocytes (**Figure 1g**). Together, the
131 ATP-dependent calcium responses and glutamate uptake confirmed generation of
132 functionally mature astrocytes.

133 To investigate how astrocytes affect neuronal function, we generated co-cultures by plating
134 hiPSC-derived cortical astrocytes and neurons in a 1:1 ratio, and cultured for at least 3 days
135 prior to use. The composition of co-cultures was assessed by immunocytochemistry using
136 both MAP2, a neuronal marker, and GFAP, an astrocytic marker (**Figure 1f, h**). The co-cultures

137 contained 55.9 ± 3.4% MAP2 positive cells and 42.9 ± 2.7% GFAP positive cells, while neuronal
138 cultures contained 93.2 ± 1.7% MAP2 positive cells and astrocytic cultures contained 90.5 ±
139 1.3% GFAP positive cells.

140 In order to generate oligomers of α-syn, human recombinant monomeric WT α-Syn was
141 aggregated in the dark at 37°C and 200 r.p.m., for ~7–8 hours. We took aliquots of α-syn
142 solution directly from an aggregation reaction at different timepoints, and we have
143 characterised them using two single molecule methods: single molecule FRET efficiency (of
144 labelled recombinant α-Syn), and single molecule aggregate visualisation by enhancement
145 (SAVE) of unlabelled recombinant α-Syn, which uses single-molecule fluorescence
146 microscopy to detect the benzothiazole salt Thioflavin-T (ThT). Upon binding to β-sheet
147 structures, ThT fluorescence increases allowing individual aggregated species to be detected.
148 At the time point selected for these experiments (end of the lag phase), the preparation is 1%
149 oligomeric, and the rest is monomer. These aggregates are smaller than 20 mers, soluble,
150 and have beta sheet conformation, and application of these aggregates to glial cells previously
151 caused TNFalpha production via TLR4 in cells, while there was no signalling from the
152 equivalent monomeric protein(*18*, *24*, *25*, *30*, *31*).

153

154 Whole cell patch-clamp recording of neurons was performed in neuron only and astro-
155 neuronal cultures to assess the electrophysiological properties and excitability of the cells. In
156 neuron only cultures, neurons (~100 DIV) displayed a relatively depolarised resting membrane
157 potential (*V*rest) compared with age-matched cells in co-cultures (–45.9 ± 2.8 mV, n = 33 vs.
158 –56.0 ± 2.1 mV, n = 34, p = 0.0053, respectively, **Supp figure 1(a,b)**). No significant difference
159 was observed in neuronal capacitance across culture types (C_m: 44.8 ± 3.5 pF, $n = 35$ in
160 cultures and 43.7 ± 3.8 pF, $n = 40$ in co-cultures, $p = 0.843$; (**Supp figure 1c**). Input resistance
161 (**Supp figure 1d**) and the time constant (**Supp figure 1e**) were significantly altered in astro-
162 neuronal cultures. In neuron only cultures, neurons generated a single action potential (AP)
163 in response to current injection, whereas neurons in astro-neuronal cultures generated a train
164 of induced APs in either step-wise depolarising protocol or slow-injecting ramp current (**Supp**
165 **figure 1f**). The parameters of AP spike (threshold, spike amplitude, kinetics) also confirmed
166 that co-cultures altered the neuronal performance. Neurons were more excitable in co-
167 cultures, as a lesser current was required to bring neurons to drive firing (**Supp figure 1g-j**).

168

169 **Single-cell RNA-sequencing of astrocyte only, neuron only and astro-neuronal cultures**

170 We used RNA-sequencing to further characterise hiPSC-derived astrocytes and neurons. After
171 120 days of differentiation all cells were harvested with and without αsyn-O stimulation, each
172 with a technical replicate resulting in 44 samples. These samples underwent bulk RNA-
173 sequencing, and six samples were also sequenced with single-cell technology (astrocyte only,
174 neuron only and astro-neuronal cultures, with and without αsyn-O). Across the integrated
175 single-cell dataset we identified 8 cell clusters, which include both astrocytic and neuronal
176 subtypes. Cell types were assigned using a set of previously published and curated marker
177 genes(*32*, *33*). Based on the expression of these marker genes, we identified two astrocytic
178 and six neuronal clusters (**Figure 1i,j**). Given that hiPSC-derived astrocytic profiles have been
179 previously well characterised by Leng and colleagues(*27*), we initially assessed our clusters for
180 correlations in gene expression globally with the reported iAstrocytes transcriptomic profiles
181 and found they were highly correlated with both of our astrocyte clusters (r = 0.71 and 0.64)
182 (**Figure 1k**), subsequently referred to as astrocyte cluster 1 (AC1) and 2 (AC2).

183 Given the growing literature on astrocytic subtypes, we investigated the clusters further.
184 Focusing specifically on genes differentially expressed between the clusters (AC1 and AC2),
185 we identified 300 genes of interest (at FDR< 5% and >2-fold change in expression) of which
186 129 were more highly expressed in AC1 and 171 genes which were more highly expressed in
187 AC2 (**Supp table 2**). Interestingly, gene set enrichment analysis of these differentially
188 expressed genes , identified immune and cytokine-related terms amongst genes more highly
189 expressed in AC1. Conversely, genes more highly expressed in AC2 showed enrichment for
190 terms related to morphogenesis, regulation of development and differentiation (**Figure 1l,**
191 **Supp table 3**). Furthermore, we noted that the pattern of gene expression in the AC2 cluster
192 appeared to resemble that described for neuroprotective astrocytes (**Supp figure 2a**). Thus,
193 we identified 2 subtypes of astrocytes, AC1 and AC2, which differed in terms of their
194 inflammatory and protective transcriptomic profiles.

195

196 **hiPSC-derived astrocytes are reactive to αsyn-O and secrete cytokines**

197 We treated astrocytes and neurons alone, and in co-culture, with fluorescently labelled
198 AF488-WT α-syn monomers at 500nM, and imaged the intracellular fluorescence over 12
199 hours. Both astrocytes and neurons alone, and in co-culture, can internalise exogenously
200 applied α-syn (**Supp figure 3ai,ii**) within 12 hours. We examined whether hiPSC-derived
201 astrocytes can induce the formation of αsyn-O using a Fluorescence Resonance Energy
202 Transfer (FRET) biosensor which enables visualisation of oligomers in cells(*25*). We treated
203 hiPSC-derived astrocytes, with two populations of fluorescently tagged α-syn (AF488- &
204 AF594-tagged A53T α-syn monomers, total 500 nM) for 24 hours, and then measured the
205 intracellular accumulation of α-syn ('total α-synuclein') based on the intensity of AF594
206 through direct excitation with 594 nm irradiation. The formation of oligomer ('FRET') was
207 visualised via the presence of signal from the acceptor fluorophore (AF594) after excitation
208 of the donor fluorophore (488 nm irradiation) (**Figure 2a**). Using this approach, we found total
209 α-syn uptake was higher in hiPSC-derived astrocytes than neurons, while similar levels of *de*
210 *novo* oligomers (FRET) were detected in both cell preparations (**Figure 2b, c**).

211 αsyn-O exposure can cause cell toxicity, and excessive ROS generation in primary
212 astrocytes(*18*). To determine whether hiPSC-derived astrocytes show similar responses, we
213 assessed ROS production using dihydroethidium (DHE) dye which allowed us to robustly
214 measure the rate of oxidation of the dye by cellular superoxide production(*34*). We found
215 that ROS production significantly increased compared to basal levels (normalised to 100%,
216 **Figure 2d, e**) in hiPSC-derived astrocytes after the application of αsyn-O. This was associated
217 with a very low level of cell death (**Figure 2f, g**).

218 Since our previous study showed that αsyn-O treatment triggers an inflammatory response in
219 primary astrocytes with associated increases in cytokine release(*18*), we assessed this
220 phenomenon in hiPSC-derived astrocytes. In agreement with our previous findings,
221 recombinant αsyn monomer, and recombinant beta-synuclein monomer did not induce an
222 inflammatory response in astrocytes (**Supp figure 3b**). We tested a range of αsyn-O
223 concentrations (100nM – 2uM), and a range of incubation times (8 hrs - 4 days) and collected
224 media and measured TNFalpha release (F**igure 2h, Supp figure 3c**).

225 Based on this data, we selected a 24 hour incubation time point, at a concentration of 1uM
226 αsyn-O (10nM oligomer), and and assessed the cytokine profiles in the media using an MSD
227 (V-PLEX Proinflammatory Panel 1) electrochemiluminescence assay kit. We found that αsyn-
228 O treatment of hiPSC-derived astrocytes consistently induced a significant increase in the
229 secretion of a variety of cytokines compared to media-only cultures. Thus, we demonstrated
230 that αsyn-O exposure induces hiPSC-derived astrocytes to become pro-inflammatory (**Figure**
231 **2h, i, j**).
232

233 **Oligomer treatment of hiPSC-derived astrocytes triggers anti-viral inflammatory responses**

234 Next, we used bulk RNA-sequencing to investigate hiPSC-derived astrocyte responses to αsyn-
235 O treatment in more detail. Given that we identified two major astrocytic clusters (AC1 and
236 AC2), we determined whether αsyn-O changes the relative proportions of these cell clusters.
237 With this in mind, we used the tool Scaden(*35*) together with our scRNA-seq data (Materials
238 and methods) to estimate cluster proportions in bulk RNA-Seq data across the whole dataset,
239 noting a high correlation in cell type proportion estimates based on single-cell and Scaden-
240 derived data (**Supp figure 2b**). This approach was based on the colocalization of all astrocytic
241 samples within exploratory principal component analyses based on bulk RNA-seq data, so
242 suggesting that the astrocyte clusters we identified in a subset of samples were in fact present
243 in all. While we found no significant change in astrocyte subtype proportion between basal
244 and αsyn-O treated astrocyte cultures (**Figure 2k, Supp table 4**), significant changes in gene
245 expression and splicing were observed.

246 We identified 2004 genes which were significantly differentially expressed (8.17% at FDR <
247 5% and at least 2-fold change in expression) following treatment of hiPSC-derived astrocytes
248 with αsyn-O, of which 917 were up-regulated and 1087 were down-regulated in the treated
249 astrocytes (**Supp table 5**). Importantly, these up-regulated genes with at least 2-fold change
250 in expression were enriched for those implicated in viral responses, including "defence
251 response to virus", "response to interferon-gamma", "type I interferon signalling pathway"
252 (**Figure 2l, Supp table 6**). These results were highly consistent with the functional data
253 demonstrating a robust cytokine response to αsyn-O treatment . Since splicing analyses have
254 been shown to provide distinct biological information(*36–38*), this form of analysis was used

255 to further characterise hiPSC-derived astrocyte responses to αsyn-O. We identified 707
256 significant differentially spliced intron clusters corresponding to 590 genes (FDR < 0.05,
257 |ΔPSI|≥ 0.1) with significant enrichment for cytoskeletal terms, potentially reflecting the
258 observed morphological changes in astrocytes with oligomer treatment (**Supp figure 3 d,e,f**
259 **& Supp tables 7,8,9**). Morphological changes induced by αsyn-O are evaluated through
260 astrocyte segmentation, followed by quantification of GFAP pixel area and intensity based on
261 the distance from the nuclear membrane. This approach assesses both morphological polarity
262 and intensity gradients(*39*, *40*), providing a detailed understanding of the spatial distribution
263 and intensity changes in astrocytic morphology thus enabling the tracking of reactive
264 astrocytic morphology upon αsyn-O stimulation.

265

266 **hiPSC-derived astrocytes maintain inflammatory states on exposure to αsyn-O in co-culture**

267 First, we studied the functional effects of αsyn-O treatment on astro-neuronal cultures. Media
268 collected from the samples were used to measure a range of cytokines secreted from the cells
269 using an MSD (V-PLEX Proinflammatory Panel 1) electrochemiluminescence assay kit. αsyn-O
270 induced more secretion of a variety of cytokines compared to untreated co-cultures
271 demonstrating inflammatory activation of the co-culture (**Figure 3a**).

272 Previously we have demonstrated that αsyn-O induced an increased level of neuronal death
273 and oxidative stress(*18*, *24*, *25*). Using live-cell imaging, we showed that activated astro-
274 neuronal cultures were associated with higher levels of cell death (**Figure 3b**), and higher
275 levels of ROS production (**Figure 3c, d**). Furthermore, patch-clamp recordings performed in
276 co-cultures treated with αsyn-O demonstrated a drop in the *V*rest after treatment (**Supp**
277 **figure 4b**) and increased input resistance (**Supp figure 4c**) in neurons. Neurons also had
278 impaired firing, with a dramatically changed AP waveform. The threshold for AP spike
279 generation was depolarised (**Supp figure 4d,e**), the amplitude was reduced (**Supp figure 4f**),
280 and the spike was significantly extended compared with control astro-neuronal cultures. Thus
281 the proteinopathy appeared to induce an activated inflammatory state of astrocytes, that is
282 associated with loss of the previous neuronal supportive function seen with resting
283 astrocytes. Additionally there are toxic gain-of-function effects in both astrocytes and

284 neurons in co-culture, such as induction of oxidative stress, altered excitability, and neuronal
285 cell death.

286 As before, we also combined single-cell and bulk RNA-sequencing analyses to assess the
287 impact of αsyn-O treatment on cell subtype proportions, gene expression and splicing. We
288 observed a significant increase in the proportion of AC1 (inflammatory) relative to AC2
289 (neuro-protective) astrocytes in αsyn-O treated as compared to co-cultures basally (**Figure**
290 **3e, Supp table 4**). We noted that there was no significant difference observed in the cell type
291 proportions of AC1 and AC2 in astrocyte only cultures on αsyn-O treatment (**Supp table 4**).
292 Differential gene expression analysis following correction for changes in predicted cell type
293 proportions, identified 774 genes (3.46%, FDR < 5% and at least 2-fold change in expression)
294 with 509 up-regulated and 265 down-regulated in the αsyn-O treated as compared to the co-
295 cultures basally (**Supp table 5**). Similar to the findings on αsyn-O treated astrocytes only, the
296 up-regulated genes with at least 2-fold change in expression were highly enriched for immune
297 response terms (**Figure 3f, Supp table 10**). As observed in the astrocyte only cultures, the
298 terms highlighted were associated with viral infections, such as "defence response to virus"
299 and "type 1 interferon signalling pathway". Furthermore, we noted that gene enrichment
300 ratios for immune-related GO terms were consistently higher in αsyn-O treated co-cultures
301 compared to astrocyte only cultures, suggesting a more prominent inflammatory response to
302 oligomer treatment in co-cultures (**Figure 3g, Supp table 11**).

303 Again, analysis of differential splicing identified distinct biological processes that were related
304 to structural organisation of cells and physical cell interactions, in contrast to gene level
305 expression signals. We identified 502 differentially spliced intron clusters in 414 genes
306 (FDR < 0.05, |ΔPSI|≥ 0.1), with the genes enriched for terms relating to junction assembly and
307 synapse (**Supp table 7**). Finally, we assessed differentially expressed and differentially spliced
308 genes for evidence of enrichment for genes genetically associated with either Mendelian
309 forms of early onset PD and Parkinsonism, or complex PD(*41*, *42*). While we did not see any
310 enrichment of Mendelian genes in astrocyte only cultures, there was significant enrichment
311 amongst all genes that were differentially expressed or differentially spliced (**Supp table 12**)
312 in astro-neuronal cultures. Overall, this suggests that this model is related to PD pathogenesis
313 and uncovers pathways related to PD causation.

314

315 **Oligomer treatment triggers *ADAR* expression and a change in isoform use**

316 αsyn-O treatment of both astrocyte only and astro-neuronal cultures resulted in the
317 activation of pathways most commonly associated with responses to viruses. In both cases,
318 we noted significant increases in the expression of genes such as *MDA5*, *RIG1* and *TLR3* that
319 can sense viral RNA (double-stranded RNA or Z-RNA)(*43–45*) and activate the release of IFN
320 and cytokines (**Figure 4a, Supp figure 5b**). This in turn is known to trigger the up-regulation
321 of a range of genes, including *OAS1*, *PKR* and *ZBP1* to degrade viral RNA, inhibit translation
322 and drive necroptosis respectively, and indeed this up-regulation was identified in αsyn-O
323 treated cultures (**Figure 4a, Supp figure 5b**).

324

325 However, these processes also undergo negative regulation by ADAR, an enzyme which
326 deaminases adenosines on double stranded RNA to inosines(*46*). This conversion reduces the
327 activation of dsRNA sensors by disrupting RNA self-complementarity and so favouring the
328 formation of single-stranded RNA forms, as well as through other direct and indirect
329 modulation of pro-inflammatory pathways(*47–50*). In fact, it is known that biallelic
330 pathogenic variants in ADAR that reduce its editing activity, result in excessive release of
331 interferons and tissue damage, and present as Aicardi Goutieres syndrome(*51*). With this in
332 mind, we noted that αsyn-O treatment of both astrocyte and astro-neuronal cultures resulted
333 in significant increases in *ADAR* expression (**Figure 4a, Supp figure 5c**) of 1.86 and 1.82 fold in
334 the cultures respectively.

335

336 Furthermore, αsyn-O treatment resulted in significant differences in transcript use (**Figure 4b,**
337 **Supp figure 5a**) as detected through splicing analyses. More specifically, we noted a decrease
338 in the use of an exon-exon junction specific to *ADAR*-201 (1:154602627-154627854:-)
339 encoding the ADAR p110 isoform, and a relative increase in the usage of an exon-exon
340 junction (1:154602627-154607991:-) specific to *ADAR*-202 encoding the p150 isoform, which
341 is already known to be under the control of an IFN-sensitive promoter (**Figure 4b, Supp figure**
342 **5a**). Thus, the functional and transcriptomic analyses of astrocyte only and astro-neuronal

343 cultures, suggest that αsyn-O treatment triggers the increased expression of *ADAR* and an
344 increase in the use of the cytoplasmic p150 isoform.

345

346

347 **αsyn-O treatment increases A-to-I editing in astrocyte-containing samples.**

348 We postulated that changes in *ADAR* expression and its isoform use would result in both an
349 increase in A-to-I editing rate and a change in the distribution of A-to-I editing sites. The latter,
350 would be expected as a consequence of the different properties of ADAR's two major
351 isoforms, with the p110 exclusively found in the nucleus and the p150 being largely
352 cytoplasmic(*52*). To investigate this we used the high-depth bulk RNA-seq data we generated
353 across all cultures to identify editing sites, in each case comparing to the reference genome.
354 Focusing on basal conditions, we detected 78,547 editing sites in astrocyte only cultures,
355 103,340 sites in the neuron only cultures, and 100,740 sites in the astro-neuronal cultures
356 (**Figure 5a**). Consistent with the known higher levels of editing in neurons(*53*), we found that
357 the median baseline editing rate at a given site was higher in neuron only (0.208) than in
358 astrocyte-containing cultures (0.054 in astrocyte only, 0.056 in astro-neuronal cultures).
359 Given that astro-neuronal cultures were composed of ~50% neurons, our findings suggest
360 that in the presence of astrocytes editing rates in neurons are lower.

361 This analysis also revealed differences in the distribution of editing sites across cell cultures.
362 In astrocyte only cultures, 50.3-59.5% of editing sites were in exonic regions, with the
363 majority of these located in the 3'UTR (49.6% and 40.9% of editing sites in astrocyte only and
364 astro-neuronal cultures, respectively **Figure 5d**). By contrast, in the neuron only cultures we
365 found that just 25.4% of sites were located in the 3'UTR. Finally, consistent with the known
366 molecular function of *ADAR* we found that irrespective of genic location or culture type, the
367 majority of editing sites (83.6 – 86.6%) were located within repeat regions, of which the vast
368 majority were in Alu regions (93.2 – 94.5%) (**Supp Figure 6c**).

369 As predicted, αsyn-O treatment generated an increase in the number of editing sites in all
370 cultures (15.8% in astrocyte only, 26.2% in neuron only, and 11.1% in astro-neuronal
371 cultures), which was highly significant (chi-squared p-value of $<2x10^{-16}$ for increased exonic

372 proportion in all cases). Similarly, measurement of editing rates at each site demonstrated
373 both a marked increase in the number of new editing sites and editing rate in astrocyte and
374 astro-neuronal cultures, but not neuron only cultures (**Figure 5b**). In contrast, across all
375 cultures relatively few editing sites were lost or had a decrease in editing rate.

376 Furthermore, consistent with a change in transcript usage, αsyn-O treatment was associated
377 with a change in the distribution of editing sites. In astrocyte-containing samples, the sites
378 with increased editing rates were significantly more likely to be in 3'UTRs than sites with
379 decreased editing (p-value < $2x10^{-16}$ in both astrocyte only and astro-neuronal cultures), while
380 in neuronal monocultures the proportion of sites in 3'UTRs did not change significantly (p-
381 value = 0.17)**.** A similar pattern was observed when exploring the biotype (as defined by
382 Ensembl VEP 93.5, RRID:SCR_002344) of the transcripts containing a given editing site, with
383 sites identified to have an increase in editing rate in astrocyte-containing cultures being more
384 likely to be located within protein coding transcripts (p-values < $8.2x10^{-8}$ and $2x10^{-16}$ in
385 astrocyte only and astro-neuronal cultures respectively, **Supp figure 6b**). Taken together,
386 these results show that αsyn-O treatment is associated with an increase in the number of
387 editing sites and differential editing rate in astrocyte-containing cultures.

388 Noting that RNA editing can influence gene expression through effects on mRNA stability, we
389 explored the relationship between transcript editing, gene expression and gene function(*54*).
390 We began by identifying all genes that both contained sites with significant differential editing
391 on exposure of cells to αsyn-O treatment, and which had significant differences in gene
392 expression in the same conditions. We found that there was a significant overlap in genes
393 that were differentially edited and differentially expressed in the astrocyte only and astro-
394 neuronal cultures following αsyn-O treatment (Fisher's exact test p-value for astrocytes
395 8.54E-4, co-culture 2.39E-2). Focusing on this gene set, namely genes that were both
396 differentially edited and expressed, we found a significant enrichment for the terms linked to
397 viral infection and immune response in both the astrocyte-containing cultures (**Figure 5e**,
398 **Supp table 13**).
399
400

401 **A-to-I RNA editing is increased in post-mortem PD brains**

402 While A-to-I editing in the human brain is well-recognised and perhaps best characterised in
403 neurons, the molecular machinery for editing is present in all the major cell types. In humans
404 A-to-I editing is catalysed not only by ADAR1 (*ADAR*), but also ADAR2 (*ADARB1*) which
405 primarily edits at conserved sites in the genome(*52*, *54*, *55*). Using publicly available snRNAseq
406 data from human brain, we confirmed the expression of *ADAR* in all major cell types including
407 astrocytes (**Figure 5f)**. In astrocytes, the majority of expression was found in the astrocytic
408 subtype expressing *VIM*, *SOX9* and *FOS*, with 19.4% of these cells expressing *ADAR*. The mean
409 expression of *ADAR* also appeared to be higher in this subgroup, with *ADAR* among the top
410 500 most expressed genes. This is in keeping with *VIM*-positive astrocytes being
411 immunoreactive, associating with response to toxins, viruses and cytokines, activation of
412 surrounding neurons, projections over extended distances in the CNS, and astro-vascular
413 interactions(*56–58*).

414 To explore whether the changes in A-to-I RNA editing seen in-vitro were also reflected in PD-
415 affected human brain tissue, we explored RNA editing in a publicly available dataset of 5
416 control and 7 PD post-mortem brain samples(*59*). Using high depth RNA-seq data generated
417 from the anterior cingulate cortex, and after controlling for covariates, we found that PD brain
418 samples had significantly higher levels of RNA editing than control samples (beta 0.011, 95%,
419 $p < 2.2 \times 10^{-16}$ CI [0.009, 0.012]). This association remained significant in a further analysis,
420 which also included the total number of editing sites per sample (beta 0.007, 95% CI [0.006,
421 0.009]). Next, we assessed the cell type specificity of the editing response. Focusing on genes
422 with the greatest increase in mean editing rate in PD (top 50 genes), we used expression
423 weighted cell type enrichment analysis(*60*) to formally assess the cell type-specificity of this
424 gene set. We found significant enrichments for multiple glial cell types, including OPCs and
425 oligodendrocytes. However, the cell type with the most significant enrichment was the
426 astrocytes (3.8 standard deviations increased from the mean, adjusted p value 0.0014),
427 suggesting that astrocytes are involved in this process in-vivo (**Figure 5g**) though not
428 exclusively.

429

430 ## Discussion

431 Astrocytes are the most abundant glial cells, supporting neuronal health and CNS immune
432 responses through multiple heterogeneous reactive and proliferative states(*61*). Whilst
433 several triggers for these states are well recognised, it remains less clear how different glial
434 states contribute in the context of diseases associated with proteinopathies. Here we
435 generated a platform of human iPSC-derived astrocytes to investigate the intersection
436 between protein aggregation as a trigger for astrocytic state switching in disease. We used a
437 serum-free small molecule approach to generate functionally active astrocytes,
438 demonstrating homeostatic calcium responses, glutamate uptake, and maturation of
439 neuronal function, as well as responses to inflammatory stimulation by canonical microglial
440 triggers (LPS). Adopting single cell sequencing to characterise the molecular identity of the
441 astrocytes revealed two astrocytic subclasses, protective and inflammatory, recapitulating
442 key astrocytic states seen in the CNS and associated with PD(*13*). Furthermore, the
443 transcriptomic signatures of our iPSC-derived astrocytes correlated highly with iPSC-derived
444 astrocytes generated by other groups(*27*). Our cellular platform may therefore be used to
445 model astrocytic states and sub-states, and uncover the mechanisms that underlie them,
446 despite the inherent limitation of their developmental fetal phenotypes(*62*).

447

448 The innate immune response recognizes pathogen- and danger-associated molecular
449 patterns (PAMPS & DAMPS) via pattern recognition receptors (including toll-like receptors
450 (TLRs), and retinoic acid-inducible gene I (RIG-I)-like receptors)(*63–65*). The role of α-syn as a
451 PAMP/DAMP is not well understood. It is currently known that α-syn may be transferred from
452 neurons to astrocytes in vitro(*66*), or from astrocytes to neurons(*67*), and several mechanisms
453 of astrocytic uptake and transfer have been proposed, including endocytosis(*68*) and
454 tunnelling nanotubes(*69*), or via Toll like receptor 2 activation enhancing the uptake of
455 fibrils(*70*). We previously demonstrated that physiological concentrations of oligomers
456 provoke an immunological response that is largely TLR4 dependent, and that glial TLR4-
457 Myd88 signalling in the substantia nigra may be causative in PD pathogenesis(*18*).

458

459 Here, we utilised the same α-syn aggregate species to reveal the downstream consequences
460 of recognition by TLRs, and the underlying mechanisms of astrocytic reactivity driven by
461 protein aggregation. Our data confirms that oligomers are recognised as DAMPS/PAMPs
462 (driven by genes *TLR3, DDX58 (*RIG-I*)).* Typically, this is followed by activation of key
463 inflammatory transcription factors, nuclear factor κB (NF-κB) and interferon regulatory
464 factors (IRFs) that induce the release of type I interferon (IFN). The initial type I IFN release
465 consequently induces the phosphorylation of IRF7, and phosphorylation of STAT2 and STAT1,
466 which forms a complex with IRF9, known as the IFN-stimulated gene factor 3 (ISGF3).
467 Oligomers induce the expression of *NFκB, IRF7, STAT1, STAT2, and ZBP1,* reflecting this
468 pathway in the hiPSC astrocytes. Finally, the DAMPS/PAMPS trigger the activation of the
469 NLRP3 inflammasome that facilitates the activation of caspase-1 and release of
470 proinflammatory cytokines interleukin-1β (IL-1β), IL-18, and pyroptosis, a sequence also
471 triggered by oligomers (*NLRP3, CASP1, IL1B)*. This transcriptomic response was mirrored
472 functionally with the morphological switch to an activated astrocyte, release of inflammatory
473 cytokines, and generation of reactive oxygen species. Moreover, in this reactive state, the
474 astrocytic supportive function of promoting neuronal activity was lost, and neuronal toxicity
475 was induced. Taken together these results suggest a mechanism whereby αsyn-O's can trigger
476 an inflammatory response in astrocytes with resulting glial and neuronal toxicity.

477

478 Intracellular double-stranded (dsRNA), evolutionarily a sign of viral infection, can also act as
479 a DAMP, and dsRNA triggers multiple cytoplasmic receptors including ZBP1, MDA5, OAS, PKR
480 which activate various arms of the innate immune cascade, including NF-κB signalling and the
481 type 1 interferon response. Of the broad changes in gene expression observed in our
482 experimental paradigm, oligomer induced type 1 interferon changes were accompanied by
483 the activation of anti-viral response pathways, with upregulation of the cytosolic double-
484 stranded nucleic acid (dsNA) sensing machinery. This machinery includes activation of the
485 negative regulator ADAR1, an enzyme that performs RNA editing, breaking the homology of
486 dsRNA, and thus dampening the immune response triggered by cytosolic dsNA and type 1
487 interferons(*46*). It is important in responding to cytosolic dsRNA that is endogenous in origin,
488 and not secondary to viral infection. From an evolutionary perspective, this process is
489 especially important in humans, where expansion of retrotransposition of non-coding

490 repetitive elements,especially alu repeats, has markedly increased the amount of
491 endogenous dsRNA within cells(*71*). The importance of the immune-dampening effect of
492 ADAR- p150 is demonstrated in loss of function mutations which result in Aicardi Goutieres
493 Syndrome, an infantile inflammatory encephalopathy which can also cause striatal necrosis,
494 a brain structure implicated in PD(*72*).

495 ADAR1 has two major isoforms, with the p110 exclusively found in the nucleus and the p150
496 being largely cytoplasmic. In the hIPSC astrocytes, we observed promoter switching with the
497 induction of the inflammatory isoform of ADAR1-p150. This resulted in a marked increase in
498 A-to-I RNA editing site number and editing rate per site, most prominently in astrocyte-
499 containing samples. The changes in editing were enriched in 3'UTRs suggesting that treatment
500 with αsyn-O resulted in a higher proportion of editing activity within the cytoplasm, where
501 ADAR1-p150 is known to localise. Furthermore, amongst genes that were both differentially
502 edited and expressed, we found a significant enrichment for terms linked to viral infection
503 and immune response in both the astrocyte-containing cultures. Thus the RNA editing is likely
504 to dampen the inflammatory response to the oligomers in vitro.

505

506 Finally we explored the role of RNA editing in PD. Using publicly available high depth RNA-seq
507 data generated from the anterior cingulate cortex from control and PD-affected individuals,
508 we found that PD brain samples had significantly higher levels of RNA editing than control
509 samples. Having identified astrocyte specificity of the RNA editing response in vitro, we
510 assessed the cell type-specificity of the editing response in vivo. Genes with the most
511 significant editing in PD were enriched in multiple glial cell types, but most significantly in
512 astrocytes, confirming the role of astrocyte RNA editing in vivo.

513 Our work raises a number of outstanding questions: how do the structural motifs of the
514 oligomers act as danger associated molecular patterns, and trigger the interferon and editing
515 response, and when does this process occur in the natural history of PD? However, most
516 importantly, is A-to-I RNA editing a beneficial compensatory response to the inflammatory
517 cascade, or does it exacerbate neurodegeneration in PD? Finally, whilst there is overlap
518 between RNA editing and the genetic risk of PD(*73*), the role of altered RNA editing in PD
519 remains unknown.

520 The findings here provide new insights into the mechanism by which inflammation may be
521 implicated in PD pathogenesis: specific protein aggregates of α-syn may act as a DAMP to
522 astrocytes, trigger inflammation and interferon like responses, which in turn triggers anti-viral
523 dsRNA responses, leading to activation of RNA editing to dampen proteinopathy induced
524 inflammatory responses. In this work, the disease specific trigger for this mechanism was the
525 beta sheet rich, soluble oligomer of α-syn. However, such mechanisms may also be triggered
526 by viral infections, which are believed to be associated with an increased risk of developing
527 PD(*74*). The identification of dsNA sensing pathways provides a potential convergent
528 mechanism between proteinopathy and viral infections in the pathogenesis of PD.

529

530 Materials and methods

531

532 Aggregation of human recombinant alpha-synuclein

533 Human recombinant α-Syn Monomeric WT or A53T α-Syn was purified from Escherichia coli
534 as previously described(*75*). Bacterial endotoxins were removed using a detoxi-gel endotoxin
535 removing Columns (ThermoFisher scientific) according to manufacturer's instruction. Levels
536 in endotoxin-free α-syn were recorded as 0.006 ng/ml (stomacher 80 biomaster seward) in α-
537 syn preparations (autoclaved endotoxin-free plastics and endotoxin-free water were used at
538 all stages of preparations). Protein was then aliquoted into separate eppendorfs into filtered
539 PBS (0.02 µM filter, Whatman) flash-frozen, stored at − 80 °C and thawed once before use. α-
540 syn oligomers were prepared by first diluting in DMEM buffer (DMEM + 1% FCS + 2 mM L-
541 glutamine). The aggregation mixture was incubated for 26.5 h at 37 °C with constant shaking
542 of 200 r.p.m (New Brunswick Scientific Innova 43, 25 mm orbital diameter) and centrifuged
543 at 14200 rpm for 10 min to remove any fibrillar pellets. We took aliquots of α-syn solution
544 directly from an aggregation reaction at different timepoints, and used in these experiments,
545 the time point, at the end of the lag phase (7-8 hours). For this time point, we generated and
546 characterised a reproducible prep of oligomers plus monomer (about 1% oligomeric; and the
547 rest is monomer). Aggregated α-syn was then stored at 4 °C until incubated with cells.

548

549 Human recombinant α-Syn monomer (Type 1) and human recombinant beta-synuclein
550 monomer were also purchased from StressMarq (for experiments shown in Supp Fig 3).

551 **hiPSc culture**

552 hiPSCs were derived from donors who had given signed informed consent as part of the EU
553 IMI-funded program StemBANCC and reprogrammed as described(*76*). Briefly, the Cyto Tune-
554 iPS reprogramming kit (Thermo Fisher Scientific) was used to reprogram fibroblasts through
555 the expression of OCT4, SOX2, KLF4 and c-MYC by four separate Sendai viral vectors. Control
556 1 (C1) and 2 (C2) were derived by StemBANCC and control 3 (C3) was purchased from Thermo
557 Fisher Scientific. Control 4 & 5 (C4 & C5) were purchased from Applied Stem Cell. hiPSCs were
558 maintained on Geltrex in Essential 8 medium (Thermo Fisher Scientific) and passaged using
559 0.5mM EDTA.

560 No iPSC lines were generated as part of this study. All iPSCs lines were obtained from a
561 number of different sources, commercially, or from repositories (part of the EU IMI-funded
562 program StemBANCC).

563 **Differentiation of hiPSC into neurons and astrocytes**

564 Differentiation of cortical region-specific astrocytes was performed using a modified protocol
565 based on Gupta et al and Seto-Salvia et al(*77*, *78*). Briefly, as demonstrated in Fig 1b, hiPSC
566 were differentiated into neural precursor cells (NPCs) using an established protocol(*79*). In
567 order to derive glial precursor cells (GPCs), NPCs were cultured with dual SMAD inhibition for
568 25-30 days, followed by culturing with the neural induction medium supplemented with 20
569 ng/ml human FGF-2)(*79*). The passage was performed twice per week (1:2 or 1:3) using
570 Accutase (Cat #A1110501, Thermo Fisher Scientific) by vigorously breaking pellets to remove
571 neuronal cells. Upon the appearance of glial morphology (around day 90 from the neural
572 induction), the GPCs were cultured for 7 days with 10 ng/ml bone morphogenetic protein 4
573 (BMP4) and 20 ng/ml leukemia inhibitory factor (LIF) which activates the JAK/STAT signalling
574 pathway, refreshing the medium every other day. On the 8th day, BMP4 and LIF were
575 withdrawn, and the GPC were further differentiated for maturation in the neural induction
576 medium without human FGF-2. 3-4 times more passages are required (1:3 or 1:4) until the
577 complete loss of the precursor property, including proliferation.

578

579 Generation of astrocytes using an adapted protocol was used to generate data on the effect
580 of monomeric in Supp Fig 3a-b(*28*).

581

582 For neurons, at around 35 days of induction, cells were dissociated into a single cell using
583 accutase and approximately 150,000 cells plated either PDL and laminin-coated glass bottom
584 8-well slide chambers (Ibidi/Thistle, cat No.80826), Geltrex coated 8-well ibidi chambers (cat
585 No. IB-80826) or 96-well plates (Falcon, cat No. 353219). Medium was replaced every 4–5
586 days and cells were used at 60–90 days after induction.

587

588 **αsyn treatment**

589 All five astrocyte lines (see Supp table 1) were split on the same day and cultured for 5 days,
590 followed by treatment with 1uM αsyn-O (equivalent of 10nM oligomer) the next day. The
591 αsyn-O preparation is generated either in buffer, or in media at a high stock concentration of
592 50µM, which is then diluted into astrocyte media to the working concentration of 1uM.
593 Therefore the αsyn-O comparisons are made to 'basal' conditions or 'media-only' in which
594 the vehicle is the media. After 24 hours of oligomer treatment, both pellets and media were
595 collected for all assays.

596 Positive controls used for astrocytic activation were performed using either LPS or TIC (TNFa:
597 30 ng/ml + IL1a: 3 ng/ml + C1q: 400 ng/ml) for 24 hours(*13*).

598

599 **Live-cell imaging**

600 Live-cell imaging was performed using an epi-fluorescence inverted microscope equipped
601 with a CCD camera (Retiga; QImaging) or confocal microscope (ZeissLSM710 or 880 with an
602 integrated metal detection system). For epi-fluorescence inverted microscope, excitation was
603 provided by a xenon arc lamp with the beam passing through a monochromator (Cairn
604 Research) and emission was reflected through a long-pass filter to a cooled CCD camera and
605 digitized to 12-bit resolution (Digital Pixel Ltd, UK) and the data were analyzed using Andor iQ
606 software (Belfast,UK). For confocal microscopes, illumination intensity was limited to 0.1-
607 0.2% of laser output to prevent phototoxicity and the pinhole was set to allow optical slice at

608 approximately 1–2µm. Pre-room temperature warmed HBSS was used as a recording buffer.
609 3–6 fields of view per well and at least 3 wells per group were used to analyze using ZEN,
610 Volocity 6.3 cellular imaging or ImageJ software. All experiments were repeated at least 2-3
611 times with different inductions.

612

613 To measure Reactive Oxygen Species (ROS, mainly superoxide), cells were washed and loaded
614 2uM dihydroethidium (HEt, Thermo Fisher Scientific) in the recording buffer. The recording
615 was performed using an epi-fluorescence inverted microscope equipped with 20x objective
616 after a quick loading in order to limit the intracellular accumulation of oxidized product and
617 the dye was present throughout the imaging. Excitation was set up to 530 nm and emission
618 recorded above 560 nm was assigned to be for the oxidized form, while excitation at 380nm
619 and emission collected from 405nm to 470nm were for the reduced form. The ratio of the
620 fluorescence intensity resulting from its oxidized/reduced forms was quantified and the rate
621 of ROS production was determined by dividing the gradient of the HEt ratio after the
622 application of recombinant α-Syn against basal gradient
623 (https://doi.org/10.5281/zenodo.14242993).

624

625 For [Ca2+]c imaging, Fura-2, AM which is a ratiometric dye with a high affinity for Ca^{2+} was
626 used. The cytosolic Ca2+as well as the rapid transient kinetics and decay times were assessed
627 (https://zenodo.org/records/10608268; https://doi.org/10.5281/zenodo.14242993). 5u
628 MFura-2 was loaded for 40 min and then washed twice before imaging. The fluorescence
629 measurement was obtained on an epifluorescence inverted microscope equipped with a 20x
630 objective. [Ca2+] was monitored in a single cell by obtaining the ratio between the excitation
631 at 340nm (high Ca2+) and 380nm (low Ca2+) for which fluorescence light was reflected
632 through a 515nm long pass filter. To trace morphological changes, Fluo4 was used and
633 recorded using confocal microscopy.

634

635 Cell death was detected using SYTOX™ Green(SYTOX, Thermo Fisher Scientific) which is
636 excluded from viable cells but exhibits red fluorescence following a loss of membrane
637 integrity and Hoechst 33342 (Hoechst, Thermo Fisher Scientific) which stains chromatin blue

638 in all cells to count the total number of cells (https://doi.org/10.5281/zenodo.14242993). 500
639 nM SYTOX and 10 uM Hoechst were directly added into the dishes, and cells were incubated
640 for 15 min. The fluorescent measurements were using confocal microscopy. Hoechst and PI
641 were excited by 405nm with the emission between 405nm and 470nm. SYTOX was excited by
642 a 488 nm laser with the emission between 488nm and 516nm. Percent cell death was
643 quantified by the percent between the number of red fluorescent cells in the total number of
644 Hoechst 33342 expressing cells per image.

645

646 **Immunocytochemistry**

647 Cells were fixed in 4% paraformaldehyde and permeabilized with 0.2% Triton-X 100. 5% BSA
648 was used to block non-specific binding before cells were incubated with primary antibodies
649 either for 2 hours at room temperature or overnight at 4°C. The next day, cells were washed
650 three times with PBS and incubated with a secondary antibody for 1hr at room temperature.
651 Cells were mounted with an antifading medium after three times wash steps (DAPI was added
652 in the second wash if required) and let dry overnight.

653 Lists of primary antibodies used; Anti-GFAP antibody (abcam, ab7260, 1:500), Anti-beta III
654 Tubulin antibody (abcam, ab78078, 1:500). Lists of secondary antibodies used;Goat Anti-
655 Chicken IgY H&L (Alexa Fluor® 488) (abcam,ab150169, 1:500), GoatAnti-Mouse IgG H&L
656 (Alexa Fluor® 555) (abcam, ab150114, 1:500).

657 **Electrophysiology**

658 Patch-clamp recordings of iPSC-derived neurons were performed using an infrared
659 differential interference contrast (DIC) imaging system on an Olympus BX51WI upright
660 microscope (Olympus, Japan) coupled with a Multipatch 700B amplifier under the control of
661 pClamp 10.2 software package (Molecular Devices, USA), as described in detail previously(*80*,
662 *81*). For the recordings, a neuronal culture or co-culture was plated on glass coverslips, placed
663 in a recording chamber mounted on the microscope stage and constantly perfused with a
664 physiological buffer medium. The perfusion medium contained (in mM) 126 NaCl, 2.5 KCl, 2
665 $MgSO_4$,2 $CaCl_2$, 26 $NaHCO_3$, 1.25 NaH_2PO4, 10 D-glucose and was continuously bubbled with
666 95% O_2 and 5% CO_2 (pH 7.4) and maintained at 30-33°C. Whole-cell recordings were
667 performed using glass pipettes with a resistance of 3.5-6 MΩ when filled with the intracellular

668 solution. This solution contained (in mM): 126 K-gluconate, 4 KCl, 4 $MgCl_2$, 2 BAPTA, 4 Mg-
669 ATP, 0.4 Na-ATP (pH 7.2, osmolarity ~295 mOsmol). In the whole-cell (immediately after
670 membrane breakthrough), iPSC-derived neurons were recorded for the resting membrane
671 potential (Vrest), membrane capacitance (Cm), the membrane time constant (τm), and input
672 resistance (Rin). To induce neuronal firing, a series of sub- and supra-threshold rectangular
673 current pulses were applied with a stepwise-increased stimulus intensity at the Vhold set at
674 −60 mV to −75 mV. The second protocol tested was a slow-ramp current injection, ramped up
675 with a 100–200 pA/s slope. The analysis of the AP waveform was performed for the first AP
676 only to quantify the threshold value, the spike amplitude, overshoot, the spike width
677 (duration at half-maximal amplitude), the rates of depolarisation and repolarisation phases
678 as previously described (https://zenodo.org/records/10608268)(*82*).

679

680 **Isolation of single cells**

681 Collecting cell pellets for bulk RNA-seq

682 To collect cell pellets, samples were trypsinised or scraped from the culture surface and
683 placed in a 15ml conical tube. These tubes were centrifuged at 800g in a refrigerated
684 centrifuge for 5 minutes, and the culture media decanted. The pellet was resuspended in 10ml
685 chilled PBS per tube by pipetting, then centrifuged again using the above parameters before
686 decanting the PBS. For bulk RNA sequencing, the cell pellets were frozen on dry ice and stored
687 at -80.

688 Collecting cell pellets for single cell RNA-seq

689 Samples for single cell RNA sequencing followed the procedure above, though instead of
690 freezing, the pellets were resuspended in 1ml PBS, and 100,000 cells were transferred to a
691 1.5ml falcon tube. These were centrifuged at 1000 rpm for 3 min at 4°C, before resuspending
692 cells in 20ul chilled DPS. 180ul chilled 100% methanol was added dropwise to the cells while
693 gently vortexing to prevent the cells from clumping, before fixing the cells on ice for 15 mins.

694

695 **Single-cell RNA-sequencing data generation and processing**

696 Between 2400 to 4000 cells were loaded for each sample into a separate channel of a
697 Chromium Chip G for use in the 10X Chromium Controller. The cells were partitioned into
698 nanoliter scale Gel Beads in emulsions (GEMs) and lysed using the 10x Genomics Single Cell
699 3' Chip V3.1 GEM, Library and Gel Bead Kit . cDNA synthesis and library construction were
700 performed as per the manufacturer's instructions. The RNA was reversed transcribed and
701 amplified using 12 cycles of PCR. Libraries were prepared from 10 µl of the cDNA and 13 cycles
702 of amplification. Each library was prepared using Single Index Kit T Set A and sequenced on
703 the HiSeq4000 system (Illumina) using 100 bp paired-end run at a mean depth of 20-50 million
704 reads per cell (EGA study id : EGAS50000000751). Libraries were generated in independent runs
705 for the different samples.

706 The reads were aligned to the human reference genome (Ensembl release 93, GRCh38) using
707 Cell Ranger v3.0.2 (Data and code availability). The analysis was carried out using Seurat
708 v3.0(*83*, *84*) following Seurat's standard workflow. Cells expressing fewer than 200 genes
709 were excluded from the subsequent analysis. In addition, we excluded cells with more than
710 3000 detected genes to remove suspected cell doublets or multiplets. Given that certain cell
711 types, e.g. neurons, naturally express higher levels of mitochondrial genes, we applied a 10%
712 cut-off for the percentage of mitochondrial genes expressed to filter out likely apoptotic cells.
713 Using default parameters of Seurat, data for each sample were log normalised across cells
714 and the 2000 most highly variable genes identified. Using the canonical correlation analysis
715 ('CCA')(*84*) to identify anchors, we integrated the samples using Seurat v3(*83*, *84*), followed
716 by regression of the effect of cell cycle and scaling of the data. Dimensional reduction was
717 performed using 50 PCs. We used Clustree v0.4.4 and Seurat's plot functions to visualise the
718 expression of astrocytic and neuronal marker genes across different cluster resolutions (0.05
719 - 0.5 in 0.05 increments and 0.5 - 1.0 in 0.1 increments)(*85*). A clustering resolution 0.25 was
720 selected, as it was the lowest resolution that explained the heterogeneity in the samples. The
721 differentially expressed genes between the clusters of interest were identified using Seurat's
722 FindMarkers() and the default 'Wilcox' test.

723

724 **Bulk tissue RNA-sequencing data generation and processing**

725 Libraries for sequencing were prepared using the Illumina TruSeq Stranded mRNA Library
726 Prep kit by loading 50 ng of total RNA into the initial reaction; fragmentation and PCR steps
727 were undertaken as per the manufacturer's instructions. Final library concentrations were
728 determined using Qubit 2.0 fluorometer and pooled to a normalized input library. Pools were
729 sequenced using the Illumina NovaSeq 6000 Sequencing system to generate 150 bp paired-
730 end reads with an average read depth of ~137 million paired-end reads per sample (EGA study
731 id : EGAS50000000751).

732 We performed pre-alignment quality control using Fastp (v 0.20.0) with default settings, for
733 adapter trimming, read filtering and base correction(*86*) (Data and code availability).
734 Processed reads were aligned to the GRCh38 human reference genome using 2-pass STAR (v
735 2.7.0a), with gene annotations from Ensembl v93(*87*, *88*). Parameters were set to match
736 ENCODE options
737 (https://github.com/RHReynolds/RNAseqProcessing/blob/master/alignment/STARmanual.p
738 df) except, we only retained uniquely mapped reads and used STAR's default of a minimum
739 3 bp overhang required for an annotated spliced alignment. Post-alignment quality metrics
740 were generated using RSeQC (v2.6.4) and MultiQC (v1.8.dev0)(*89*, *90*). We found that an
741 average of 90.4% reads were uniquely mapped.

742 The processed reads were also quantified with Salmon (v 0.14.1) using the mapping-based
743 mode with a decoy-aware transcriptome based on GRCh38 and Ensembl v93 as the
744 reference(*91*). Salmon's options correcting for sequence, non-uniform coverage biases
745 (including 5' or 3' bias) and GC bias in the data were enabled and the R package tximport used
746 to transform Salmon transcript-level abundance estimates to gene-level values(*92*). Pipeline
747 source code can be found in https://github.com/RHReynolds/RNAseqProcessing.

748 **Deconvolution**

749 Cell type proportions in the bulk tissue RNA-sequencing samples were estimated using Scaden
750 (v1.1.2)(*35*). Scaden trains on simulated bulk RNA-sequencing samples, generated from
751 tissue-specific single cell data, and predicts cell type proportions in bulk tissue RNA-
752 sequencing data. The training data was generated using the raw counts and cell types based
753 on the clustering 0.25 from the single cell data. Thereby we created 2,000 artificial bulk tissue

754 RNA-sequencing samples by randomly selecting 3,000 cells from the total of 8,132 cells .
755 Prediction of the cell type proportions were made using the default parameters and the
756 Scaden developers' recommendations. Following deconvolution, significant differences in the
757 cell type proportions between the αsyn-O treated and basal astrocytes and co-culture were
758 investigated using a paired t-test and multiple comparison correction using Benjamini &
759 Hochberg method, per cell culture. This was only applied to cell types with proportions >=
760 0.01, which included Astrocyte clusters 1 and 2 and Neuron clusters 1, 2 and 3.

761 **Differential gene expression analysis**

762 Sources of variation in bulk tissue RNA-sequencing data were assessed by performing
763 principal component analysis on the gene level expression filtered to include genes expressed
764 in all samples of each cell culture and treatment.

765 We found that cell culture and cell-type proportions were significantly correlated with the
766 first PC (Supp fig. 3b). The individual, age and sex correlated with PC2. Individual, RIN and
767 astrocyte cluster 2 correlated with PC3, while culture, individual, age and neuron cluster 5
768 were significantly correlated with PC4. The treatment applied to the cell culture correlated
769 with PC5. Accordingly, PC axes 2, 3 and 4 were included as covariates in the model for
770 differential expression and splicing analyses of the bulk-tissue RNA-sequencing data. Bulk-
771 tissue differential gene expression was examined using DESeq2 (v1.30.1)(*93*), including only
772 genes expressed in all samples within a cell culture and treatment group, collapsing across
773 individuals in a cell culture and treatment group; and controlling for covariates. FDR-
774 correction for multiple testing was performed using the Benjamini and Hochberg method, and
775 a cut-off of FDR < 5% was used to consider a gene as significantly differentially expressed.

776

777 **Differential splicing analysis**

778 Differential splicing analysis was conducted using Leafcutter (v0.2.9)(*94*). It detects changes
779 in alternative splicing events by constructing clusters of introns that share splice sites and
780 determining the difference in intron usage, measuring differential splicing in terms of the
781 change in the percent spliced in (ΔPSI). Splice junctions outputted by STAR were filtered to
782 remove those with length < 25 nucleotides and regions that overlapped the ENCODE blacklist
783 regions (https://github.com/Boyle-Lab/Blacklist/tree/master/lists)(*95*). The junctions were

784 annotated using junction_annot() from dasper(*96*), classifying them into the following
785 categories, (based on if one end (acceptor or donor) or both ends match the boundary of a
786 known exon) - annotated, novel acceptor, novel donor, novel combination, novel exon skip,
787 unannotated and ambiguous gene (mapped to more than 1 gene). Those annotated as
788 ambiguous were excluded from this analysis. Leafcutter was run to identify intron clusters by
789 excluding introns of length greater than 1 Mb and those that were supported by < 30 junction
790 reads across all the samples or < 0.1% of the total number of junction read counts for the
791 entire cluster. Differentially spliced clusters were identified pairwise, in treated vs untreated
792 astrocytes and co-culture samples, using leafcutter's default parameters and controlling for
793 covariates as identified by the gene level expression. 40,892 and 44,390 clusters (that lie in a
794 single gene) were successfully tested for differential splicing in the astrocytes treated vs
795 untreated and co-culture treated vs untreated respectively. Multiple testing correction via
796 FDR estimation was done, with an intron cluster and its overlapping gene considered
797 differentially spliced at FDR < 0.05 and if the intron cluster contained at least one intron with
798 an absolute delta percent spliced-in value ($|\Delta PSI|$) ≥ 0.1. Functional enrichment analysis was
799 performed using clusterProfiler (v3.18.1)(*97*). Gene ontology over-representation analyses
800 were run and comparisons between genelists made using compareCluster(). FDR-correction
801 for multiple testing was done and terms with FDR < 0.05 were considered significant. We
802 analysed differentially expressed genes at FDR < 5% and with at least >= 2 fold change in
803 expression and differentially spliced genes at FDR < 5% and $|\Delta PSI| \geq 0.1$.

804 ADAR's differentially spliced transcripts were linked to the protein isoforms by first identifying
805 the transcripts the differentially spliced junctions overlapped with. The junctions overlapped
806 with transcripts ADAR-201 and ADAR-202. The number of amino acids in these transcripts
807 matched to P55265-5 (synonym p110) and P55265-1 (synonym p150) in Uniprot(*98*)
808 respectively. We further ran multiple sequence alignment of the amino acid sequences from
809 UniProt and Ensembl (obtained from the in silico translated mRNA is translated) for each of
810 the isoforms, that was a match. ADAR's differentially spliced junctions were visualised with
811 ADAR's protein coding transcript structures using ggtranscript(*99*).

812

813 **A-to-I editing**

814 RNA editing analysis was undertaken with JACUSA2 v2.0.2 (https://github.com/dieterich-
815 lab/JACUSA2), leveraging GNU parallel v20230722
816 (https://www.gnu.org/software/parallel/)(*100–102*). This utilises a drichilet multinomial
817 distribution to ascertain whether transcripts are edited at a genomic site in two modes: in
818 'detect' mode it compares transcripts against a reference genome identifying editing in
819 individual samples; in 'differential' mode it will compare two samples against each other,
820 looking at sites that are differentially edited in one sample compared to another. Noting that
821 transcripts with increased editing might not be successfully mapped during the alignment
822 step, multi-sample 2-pass mapping with STAR v2.7.9a
823 (https://code.google.com/archive/p/rna-star/) was re-run, allowing a more generous
824 mismatch rate of 16 base pairs per 100(*87*). This did not increase the rate of multimapping
825 during alignment**.** PCR duplicates were identified by samtools v1.13 markdup
826 (https://www.htslib.org)(*103*). A-to-I editing was assessed in properly paired, non-duplicate
827 reads, with settings to exclude any potential editing sites near the start and end of reads,
828 indel positions and splice sites, as well as sites within homopolymer runs of more than 7 bases.
829 An editing site was considered significant if it had an absolute z score greater than 1.96 ($|z|$
830 ≥ 1.96). Replicates for each sample group were input to JACUSA2 detect to output a list of
831 editing sites for each of the six groups: astrocytes untreated, astrocytes treated, co-culture
832 untreated, co-culture treated, neuron untreated and neuron treated. Differences in editing
833 sites and rates were explored using R (v 4.2, www.r-project.org). JACUSA2 differential was
834 used to ascertain those sites that were differentially edited in treated samples of each cell
835 line, compared to untreated. Edits were annotated with Ensembl's variant effect predictor
836 (VEP, v93.5, https://www.ensembl.org/info/docs/tools/vep), filtering duplicate results by
837 consequence, and biotypes of interest(*104*). Where results were not derived with Ensembl
838 VEP, a manual annotation was undertaken using the Ensembl GTF file, deriving genic location
839 and biotype. Editing sites were also annotated with repeat motifs downloaded from
840 RepeatMasker v4.0.5 (http://www.repeatmasker.org/)(*105*). Functional enrichment of the
841 differentially edited genes (FDR< 5%) that were also differentially expressed (FDR< 5% & at
842 least 2 fold change in expression) was examined using clusterprofiler (v3.18.1)(*97*).

843 **Post-mortem brain editing analysis**

844 Post-mortem human brain samples were sourced from publicly available data, including bulk
845 and single-nuclear RNA sequencing data from 5 control and 7 PD anterior cingulate cortex
846 samples from donors with Braak stage 5-6 disease (https://ega-archive.org/ study ID:
847 EGAS00001005305; https://www.ncbi.nlm.nih.gov/geo/ accession ID: GSE178146)(*106*).
848 Single-nuclear gene expression was explored in python 3.9 (www.python.org) using the
849 pl.dotplot function from scanpy 1.7.2(*107*). As with the cellular models, bulk transcriptomic
850 samples were passed through the editing pipeline including trimming with fastp, and
851 alignment with STAR allowing 16 base mismatches per 100, and then identification of editing
852 sites using JACUSA2 as above. Using R 4.2.0, sites were filtered to include those present in at
853 least 2 samples per PD and control group, and presence in both groups. Sites with editing rate
854 greater than 0 and less than 1 were input into a linear regression as follows: Editing_rate ~
855 Disease_Group + Sex + RIN. Expression weighted celltype enrichment (EWCE v1.11.3,
856 nathanskene.github.io/EWCE/index.html) analysis was undertaken using specificity matrices
857 previously derived for this dataset from single nuclear RNA sequencing results(*60*, *106*). The
858 ranked gene list input to EWCE was defined by the genes with the greatest increase in mean
859 editing rate, relative to all the genes where editing was detected including genes with editing
860 rate of 1.

861

862 # Bibliography

863

864 1. H. Braak, K. Del Tredici, U. Rüb, R. A. I. de Vos, E. N. H. Jansen Steur, E. Braak, Staging
865 of brain pathology related to sporadic Parkinson's disease. *Neurobiol. Aging* **24**, 197–
866 211 (2003).
867 2. P. Damier, E. C. Hirsch, P. Zhang, Y. Agid, F. Javoy-Agid, Glutathione peroxidase, glial
868 cells and Parkinson's disease. *Neuroscience* **52**, 1–6 (1993).
869 3. C. Knott, G. P. Wilkin, G. Stern, Astrocytes and microglia in the substantia nigra and
870 caudate-putamen in Parkinson's disease. *Parkinsonism Relat. Disord.* **5**, 115–122
871 (1999).
872 4. D.-K. Choi, S. Pennathur, C. Perier, K. Tieu, P. Teismann, D.-C. Wu, V. Jackson-Lewis,
873 M. Vila, J.-P. Vonsattel, J. W. Heinecke, S. Przedborski, Ablation of the Inflammatory
874 Enzyme Myeloperoxidase Mitigates Features of Parkinson's Disease in Mice. *J.*
875 *Neurosci.* **25**, 6594–6600 (2005).
876 5. J. Miklossy, D. D. Doudet, C. Schwab, S. Yu, E. G. McGeer, P. L. McGeer, Role of ICAM-
877 1 in persisting inflammation in Parkinson disease and MPTP monkeys. *Exp. Neurol.*

878 **197**, 275–283 (2006).
879 6. I. Lastres-Becker, A. Ulusoy, N. G. Innamorato, G. Sahin, A. Rábano, D. Kirik, A.
880 Cuadrado, α-Synuclein expression and Nrf2 deficiency cooperate to aggravate protein
881 aggregation, neuronal death and inflammation in early-stage Parkinson's disease.
882 *Hum. Mol. Genet.* **21**, 3173–3192 (2012).
883 7. K. Sathe, W. Maetzler, J. D. Lang, R. B. Mounsey, C. Fleckenstein, H. L. Martin, C.
884 Schulte, S. Mustafa, M. Synofzik, Z. Vukovic, S. Itohara, D. Berg, P. Teismann, S100B is
885 increased in Parkinson's disease and ablation protects against MPTP-induced toxicity
886 through the RAGE and TNF-α pathway. *Brain* **135**, 3336–3347 (2012).
887 8. Z. A. Sorrentino, Y. Xia, C. Funk, C. J. Riffe, N. J. Rutherford, C. Ceballos Diaz, A. N.
888 Sacino, N. D. Price, T. E. Golde, B. I. Giasson, P. Chakrabarty, Motor neuron loss and
889 neuroinflammation in a model of α-synuclein-induced neurodegeneration. *Neurobiol.*
890 *Dis.* **120**, 98–106 (2018).
891 9. A. J. Schaser, T. L. Stackhouse, L. J. Weston, P. C. Kerstein, V. R. Osterberg, C. S. López,
892 D. W. Dickson, K. C. Luk, C. K. Meshul, R. L. Woltjer, V. K. Unni, Trans-synaptic and
893 retrograde axonal spread of Lewy pathology following pre-formed fibril injection in an
894 in vivo A53T alpha-synuclein mouse model of synucleinopathy. *Acta Neuropathol.*
895 *Commun.* **8**, 150 (2020).
896 10. M. F. Altay, A. K. L. Liu, J. L. Holton, L. Parkkinen, H. A. Lashuel, Prominent astrocytic
897 alpha-synuclein pathology with unique post-translational modification signatures
898 unveiled across Lewy body disorders. *Acta Neuropathol. Commun.* **10**, 163 (2022).
899 11. F. Weiss, A. Labrador-Garrido, N. Dzamko, G. Halliday, Immune responses in the
900 Parkinson's disease brain. *Neurobiol. Dis.* **168**, 105700 (2022).
901 12. H.-G. Lee, M. A. Wheeler, F. J. Quintana, Function and therapeutic value of astrocytes
902 in neurological diseases. *Nat. Rev. Drug Discov.* **21**, 339–358 (2022).
903 13. S. A. Liddelow, K. A. Guttenplan, L. E. Clarke, F. C. Bennett, C. J. Bohlen, L. Schirmer,
904 M. L. Bennett, A. E. Münch, W.-S. Chung, T. C. Peterson, D. K. Wilton, A. Frouin, B. A.
905 Napier, N. Panicker, M. Kumar, M. S. Buckwalter, D. H. Rowitch, V. L. Dawson, T. M.
906 Dawson, B. Stevens, B. A. Barres, Neurotoxic reactive astrocytes are induced by
907 activated microglia. *Nature* **541**, 481–487 (2017).
908 14. L. Barbar, T. Jain, M. Zimmer, I. Kruglikov, J. S. Sadick, M. Wang, K. Kalpana, I. V. L.
909 Rose, S. R. Burstein, T. Rusielewicz, M. Nijsure, K. A. Guttenplan, A. di Domenico, G.
910 Croft, B. Zhang, H. Nobuta, J. M. Hébert, S. A. Liddelow, V. Fossati, CD49f Is a Novel
911 Marker of Functional and Reactive Human iPSC-Derived Astrocytes. *Neuron* **107**, 436-
912 453.e12 (2020).
913 15. J. S. Sadick, M. R. O'Dea, P. Hasel, T. Dykstra, A. Faustin, S. A. Liddelow, Astrocytes and
914 oligodendrocytes undergo subtype-specific transcriptional changes in Alzheimer's
915 disease. *Neuron* **110**, 1788-1805.e10 (2022).
916 16. E. Shigetomi, S. Patel, B. S. Khakh, Probing the Complexities of Astrocyte Calcium
917 Signaling. *Trends Cell Biol.* **26**, 300–312 (2016).
918 17. C. Escartin, E. Galea, A. Lakatos, J. P. O'Callaghan, G. C. Petzold, A. Serrano-Pozo, C.
919 Steinhäuser, A. Volterra, G. Carmignoto, A. Agarwal, N. J. Allen, A. Araque, L. Barbeito,
920 A. Barzilai, D. E. Bergles, G. Bonvento, A. M. Butt, W.-T. Chen, M. Cohen-Salmon, C.
921 Cunningham, B. Deneen, B. De Strooper, B. Díaz-Castro, C. Farina, M. Freeman, V.
922 Gallo, J. E. Goldman, S. A. Goldman, M. Götz, A. Gutiérrez, P. G. Haydon, D. H.
923 Heiland, E. M. Hol, M. G. Holt, M. Iino, K. V. Kastanenka, H. Kettenmann, B. S. Khakh,
924 S. Koizumi, C. J. Lee, S. A. Liddelow, B. A. MacVicar, P. Magistretti, A. Messing, A.

Mishra, A. V. Molofsky, K. K. Murai, C. M. Norris, S. Okada, S. H. R. Oliet, J. F. Oliveira, A. Panatier, V. Parpura, M. Pekna, M. Pekny, L. Pellerin, G. Perea, B. G. Pérez-Nievas, F. W. Pfrieger, K. E. Poskanzer, F. J. Quintana, R. M. Ransohoff, M. Riquelme-Perez, S. Robel, C. R. Rose, J. D. Rothstein, N. Rouach, D. H. Rowitch, A. Semyanov, S. Sirko, H. Sontheimer, R. A. Swanson, J. Vitorica, I.-B. Wanner, L. B. Wood, J. Wu, B. Zheng, E. R. Zimmer, R. Zorec, M. V. Sofroniew, A. Verkhratsky, Reactive astrocyte nomenclature, definitions, and future directions. *Nat. Neurosci.* **24**, 312–325 (2021).

18. C. D. Hughes, M. L. Choi, M. Ryten, L. Hopkins, A. Drews, J. A. Botía, M. Iljina, M. Rodrigues, S. A. Gagliano, S. Gandhi, C. Bryant, D. Klenerman, Picomolar concentrations of oligomeric alpha-synuclein sensitizes TLR4 to play an initiating role in Parkinson's disease pathogenesis. *Acta Neuropathol. (Berl.)* **137**, 103–120 (2019).
19. S. P. Yun, T.-I. Kam, N. Panicker, S. Kim, Y. Oh, J.-S. Park, S.-H. Kwon, Y. J. Park, S. S. Karuppagounder, H. Park, S. Kim, N. Oh, N. A. Kim, S. Lee, S. Brahmachari, X. Mao, J. H. Lee, M. Kumar, D. An, S.-U. Kang, Y. Lee, K. C. Lee, D. H. Na, D. Kim, S. H. Lee, V. V. Roschke, S. A. Liddelow, Z. Mari, B. A. Barres, V. L. Dawson, S. Lee, T. M. Dawson, H. S. Ko, Block of A1 astrocyte conversion by microglia is neuroprotective in models of Parkinson's disease. *Nat. Med.* **24**, 931–938 (2018).
20. P. Hasel, I. V. L. Rose, J. S. Sadick, R. D. Kim, S. A. Liddelow, Neuroinflammatory astrocyte subtypes in the mouse brain. *Nat. Neurosci.* **24**, 1475–1487 (2021).
21. K. Russ, G. Teku, L. Bousset, V. Redeker, S. Piel, E. Savchenko, Y. Pomeshchik, J. Savistchenko, T. C. Stummann, C. Azevedo, A. Collin, S. Goldwurm, K. Fog, E. Elmer, M. Vihinen, R. Melki, L. Roybon, TNF-α and α-synuclein fibrils differently regulate human astrocyte immune reactivity and impair mitochondrial respiration. *Cell Rep.* **34**, 108895 (2021).
22. J. Rostami, G. Fotaki, J. Sirois, R. Mzezewa, J. Bergström, M. Essand, L. Healy, A. Erlandsson, Astrocytes have the capacity to act as antigen-presenting cells in the Parkinson's disease brain. *J. Neuroinflammation* **17**, 119 (2020).
23. N. Bengoa-Vergniory, R. F. Roberts, R. Wade-Martins, J. Alegre-Abarrategui, Alpha-synuclein oligomers: a new hope. *Acta Neuropathol. (Berl.)* **134**, 819–838 (2017).
24. P. R. Angelova, M. L. Choi, A. V. Berezhnov, M. H. Horrocks, C. D. Hughes, S. De, M. Rodrigues, R. Yapom, D. Little, K. S. Dolt, T. Kunath, M. J. Devine, P. Gissen, M. S. Shchepinov, S. Sylantyev, E. V. Pavlov, D. Klenerman, A. Y. Abramov, S. Gandhi, Alpha synuclein aggregation drives ferroptosis: an interplay of iron, calcium and lipid peroxidation. *Cell Death Differ.* **27**, 2781–2796 (2020).
25. M. L. Choi, A. Chappard, B. P. Singh, C. Maclachlan, M. Rodrigues, E. I. Fedotova, A. V. Berezhnov, S. De, C. J. Peddie, D. Athauda, G. S. Virdi, W. Zhang, J. R. Evans, A. I. Wernick, Z. S. Zanjani, P. R. Angelova, N. Esteras, A. Y. Vinokurov, K. Morris, K. Jeacock, L. Tosatto, D. Little, P. Gissen, D. J. Clarke, T. Kunath, L. Collinson, D. Klenerman, A. Y. Abramov, M. H. Horrocks, S. Gandhi, Pathological structural conversion of α-synuclein at the mitochondria induces neuronal toxicity. *Nat. Neurosci.* **25**, 1134–1148 (2022).
26. E. Deas, N. Cremades, P. R. Angelova, M. H. R. Ludtmann, Z. Yao, S. Chen, M. H. Horrocks, B. Banushi, D. Little, M. J. Devine, P. Gissen, D. Klenerman, C. M. Dobson, N. W. Wood, S. Gandhi, A. Y. Abramov, Alpha-Synuclein Oligomers Interact with Metal Ions to Induce Oxidative Stress and Neuronal Death in Parkinson's Disease. *Antioxid. Redox Signal.* **24**, 376–391 (2016).
27. K. Leng, I. V. L. Rose, H. Kim, W. Xia, W. Romero-Fernandez, B. Rooney, M. Koontz, E.

Li, Y. Ao, S. Wang, M. Krawczyk, J. Tcw, A. Goate, Y. Zhang, E. M. Ullian, M. V. Sofroniew, S. P. J. Fancy, M. S. Schrag, E. S. Lippmann, M. Kampmann, CRISPRi screens in human iPSC-derived astrocytes elucidate regulators of distinct inflammatory reactive states. *Nat. Neurosci.* **25**, 1528–1542 (2022).

28. B. E. Clarke, D. M. Taha, O. J. Ziff, A. Alam, E. P. Thelin, N. M. García, A. Helmy, R. Patani, Human stem cell-derived astrocytes exhibit region-specific heterogeneity in their secretory profiles. *Brain* **143**, e85 (2020).

29. C. E. Hall, Z. Yao, M. Choi, G. E. Tyzack, A. Serio, R. Luisier, J. Harley, E. Preza, C. Arber, S. J. Crisp, P. M. D. Watson, D. M. Kullmann, A. Y. Abramov, S. Wray, R. Burley, S. H. Y. Loh, L. M. Martins, M. M. Stevens, N. M. Luscombe, C. R. Sibley, A. Lakatos, J. Ule, S. Gandhi, R. Patani, Progressive Motor Neuron Pathology and the Role of Astrocytes in a Human Stem Cell Model of VCP-Related ALS. *Cell Rep.* **19**, 1739–1749 (2017).

30. M. H. R. Ludtmann, P. R. Angelova, M. H. Horrocks, M. L. Choi, M. Rodrigues, A. Y. Baev, A. V. Berezhnov, Z. Yao, D. Little, B. Banushi, A. S. Al-Menhali, R. T. Ranasinghe, D. R. Whiten, R. Yapom, K. S. Dolt, M. J. Devine, P. Gissen, T. Kunath, M. Jaganjac, E. V. Pavlov, D. Klenerman, A. Y. Abramov, S. Gandhi, α-synuclein oligomers interact with ATP synthase and open the permeability transition pore in Parkinson's disease. *Nat. Commun.* **9**, 2293 (2018).

31. K. D'Sa, J. R. Evans, G. S. Virdi, G. Vecchi, A. Adam, O. Bertolli, J. Fleming, H. Chang, C. Leighton, M. H. Horrocks, D. Athauda, M. L. Choi, S. Gandhi, Prediction of mechanistic subtypes of Parkinson's using patient-derived stem cell models. *Nat. Mach. Intell.* **5**, 933–946 (2023).

32. D. Wang, S. Liu, J. Warrell, H. Won, X. Shi, F. C. P. Navarro, D. Clarke, M. Gu, P. Emani, Y. T. Yang, M. Xu, M. J. Gandal, S. Lou, J. Zhang, J. J. Park, C. Yan, S. K. Rhie, K. Manakongtreecheep, H. Zhou, A. Nathan, M. Peters, E. Mattei, D. Fitzgerald, T. Brunetti, J. Moore, Y. Jiang, K. Girdhar, G. E. Hoffman, S. Kalayci, Z. H. Gümüş, G. E. Crawford, PsychENCODE Consortium, P. Roussos, S. Akbarian, A. E. Jaffe, K. P. White, Z. Weng, N. Sestan, D. H. Geschwind, J. A. Knowles, M. B. Gerstein, Comprehensive functional genomic resource and integrative model for the human brain. *Science* **362** (2018).

33. A. Zeisel, A. B. Muñoz-Manchado, S. Codeluppi, P. Lönnerberg, G. La Manno, A. Juréus, S. Marques, H. Munguba, L. He, C. Betsholtz, C. Rolny, G. Castelo-Branco, J. Hjerling-Leffler, S. Linnarsson, Cell types in the mouse cortex and hippocampus revealed by single-cell RNA-seq. *Science* **347**, 1138–1142 (2015).

34. Measuring reactive species and oxidative damage in vivo and in cell culture: how should you do it and what do the results mean? - Halliwell - 2004 - British Journal of Pharmacology - Wiley Online Library. https://bpspubs.onlinelibrary.wiley.com/doi/full/10.1038/sj.bjp.0705776.

35. K. Menden, M. Marouf, S. Oller, A. Dalmia, D. S. Magruder, K. Kloiber, P. Heutink, S. Bonn, Deep learning–based cell composition analysis from tissue expression profiles. *Sci. Adv.* **6**, eaba2619 (2020).

36. A. G. L. Douglas, M. J. A. Wood, RNA splicing: disease and therapy. *Brief. Funct. Genomics* **10**, 151–164 (2011).

37. M. M. Scotti, M. S. Swanson, RNA mis-splicing in disease. *Nat. Rev. Genet.* **17**, 19–32 (2016).

38. S. García-Ruiz, E. K. Gustavsson, D. Zhang, R. H. Reynolds, Z. Chen, A. Fairbrother-Browne, A. L. Gil-Martínez, J. A. Botia, L. Collado-Torres, M. Ryten, IntroVerse: a

1019 comprehensive database of introns across human tissues. *Nucleic Acids Res.* **51**,
1020 D167–D178 (2023).
1021 39. M. J. Raymond, P. Ray, G. Kaur, M. Fredericks, A. V. Singh, L. Q. Wan, Multiaxial
1022 Polarity Determines Individual Cellular and Nuclear Chirality. *Cell. Mol. Bioeng.* **10**,
1023 63–74 (2017).
1024 40. Z. Zhang, K. C. M. Lee, D. M. D. Siu, M. C. K. Lo, Q. T. K. Lai, E. Y. Lam, K. K. Tsia,
1025 Morphological profiling by high-throughput single-cell biophysical fractometry.
1026 *Commun. Biol.* **6**, 1–13 (2023).
1027 41. A. R. Martin, E. Williams, R. E. Foulger, S. Leigh, L. C. Daugherty, O. Niblock, I. U. S.
1028 Leong, K. R. Smith, O. Gerasimenko, E. Haraldsdottir, E. Thomas, R. H. Scott, E. Baple,
1029 A. Tucci, H. Brittain, A. de Burca, K. Ibañez, D. Kasperaviciute, D. Smedley, M.
1030 Caulfield, A. Rendon, E. M. McDonagh, PanelApp crowdsources expert knowledge to
1031 establish consensus diagnostic gene panels. *Nat. Genet.* **51**, 1560–1565 (2019).
1032 42. M. A. Nalls, C. Blauwendraat, C. L. Vallerga, K. Heilbron, S. Bandres-Ciga, D. Chang, M.
1033 Tan, D. A. Kia, A. J. Noyce, A. Xue, J. Bras, E. Young, R. von Coelln, J. Simón-Sánchez, C.
1034 Schulte, M. Sharma, L. Krohn, L. Pihlstrøm, A. Siitonen, H. Iwaki, H. Leonard, F. Faghri,
1035 J. R. Gibbs, D. G. Hernandez, S. W. Scholz, J. A. Botia, M. Martinez, J.-C. Corvol, S.
1036 Lesage, J. Jankovic, L. M. Shulman, M. Sutherland, P. Tienari, K. Majamaa, M. Toft, O.
1037 A. Andreassen, T. Bangale, A. Brice, J. Yang, Z. Gan-Or, T. Gasser, P. Heutink, J. M.
1038 Shulman, N. W. Wood, D. A. Hinds, J. A. Hardy, H. R. Morris, J. Gratten, P. M. Visscher,
1039 R. R. Graham, A. B. Singleton, 23andMe Research Team, System Genomics of
1040 Parkinson's Disease Consortium, International Parkinson's Disease Genomics
1041 Consortium, Identification of novel risk loci, causal insights, and heritable risk for
1042 Parkinson's disease: a meta-analysis of genome-wide association studies. *Lancet*
1043 *Neurol.* **18**, 1091–1102 (2019).
1044 43. J. Quin, J. Sedmík, D. Vukić, A. Khan, L. P. Keegan, M. A. O'Connell, ADAR RNA
1045 Modifications, the Epitranscriptome and Innate Immunity. *Trends Biochem. Sci.* **46**,
1046 758–771 (2021).
1047 44. Y. G. Chen, S. Hur, Cellular origins of dsRNA, their recognition and consequences. *Nat.*
1048 *Rev. Mol. Cell Biol.* **23**, 286–301 (2022).
1049 45. Y. Hao, B. Yang, J. Yang, X. Shi, X. Yang, D. Zhang, D. Zhao, W. Yan, L. Chen, H. Zheng,
1050 K. Zhang, X. Liu, ZBP1: A Powerful Innate Immune Sensor and Double-Edged Sword in
1051 Host Immunity. *Int. J. Mol. Sci.* **23**, 10224 (2022).
1052 46. K. Nishikura, Functions and regulation of RNA editing by ADAR deaminases. *Annu.*
1053 *Rev. Biochem.* **79**, 321–349 (2010).
1054 47. K. A. Cottrell, R. J. Andrews, B. L. Bass, The competitive landscape of the dsRNA world.
1055 *Mol. Cell* **84**, 107–119 (2024).
1056 48. K. Sinigaglia, A. Cherian, D. Vukic, J. Melicherova, P. Linhartova, Q. Du, L. Zerad, S.
1057 Stejskal, R. Malik, J. Prochazka, N. Bondurand, R. Sedlacek, M. A. O'Connell, L. P.
1058 Keegan, "Aberrant activation of the innate immune sensor PKR by self dsRNA is
1059 prevented by direct interaction with ADAR1" (preprint, Immunology, 2023);
1060 https://doi.org/10.1101/2023.08.29.555105.
1061 49. S. Zhou, C. Yang, F. Zhao, Y. Huang, Y. Lin, C. Huang, X. Ma, J. Du, Y. Wang, G. Long, J.
1062 He, C. Liu, P. Zhang, Double-stranded RNA deaminase ADAR1 promotes the Zika virus
1063 replication by inhibiting the activation of protein kinase PKR. *J. Biol. Chem.* **294**,
1064 18168–18180 (2019).
1065 50. A. D. J. Scadden, Inosine-containing dsRNA binds a stress-granule-like complex and

1066 downregulates gene expression in trans. *Mol. Cell* **28**, 491–500 (2007).
1067 51. Y. J. Crow, N. Manel, Aicardi–Goutières syndrome and the type I interferonopathies.
1068 *Nat. Rev. Immunol.* **15**, 429–440 (2015).
1069 52. A. Gallo, D. Vukic, D. Michalík, M. A. O'Connell, L. P. Keegan, ADAR RNA editing in
1070 human disease; more to it than meets the I. *Hum. Genet.* **136**, 1265–1278 (2017).
1071 53. W. H. Cuddleston, J. Li, X. Fan, A. Kozenkov, M. Lalli, S. Khalique, S. Dracheva, E. A.
1072 Mukamel, M. S. Breen, Cellular and genetic drivers of RNA editing variation in the
1073 human brain. *Nat. Commun.* **13**, 2997 (2022).
1074 54. I. X. Wang, E. So, J. L. Devlin, Y. Zhao, M. Wu, V. G. Cheung, ADAR regulates RNA
1075 editing, transcript stability, and gene expression. *Cell Rep.* **5**, 849–860 (2013).
1076 55. K. Hajji, J. Sedmík, A. Cherian, D. Amoruso, L. P. Keegan, M. A. O'Connell, ADAR2
1077 enzymes: efficient site-specific RNA editors with gene therapy aspirations. *RNA N. Y.*
1078 **28**, 1281–1297 (2022).
1079 56. L. A. O'Leary, M. A. Davoli, C. Belliveau, A. Tanti, J. C. Ma, W. T. Farmer, G. Turecki, K.
1080 K. Murai, N. Mechawar, Characterization of Vimentin-Immunoreactive Astrocytes in
1081 the Human Brain. *Front. Neuroanat.* **14** (2020).
1082 57. F. Cruz-Mendoza, F. Jauregui-Huerta, A. Aguilar-Delgadillo, J. García-Estrada, S.
1083 Luquin, Immediate Early Gene c-fos in the Brain: Focus on Glial Cells. *Brain Sci.* **12**, 687
1084 (2022).
1085 58. E. K. Erickson, A. J. DaCosta, S. C. Mason, Y. A. Blednov, R. D. Mayfield, R. A. Harris,
1086 Cortical astrocytes regulate ethanol consumption and intoxication in mice.
1087 *Neuropsychopharmacology* **46**, 500–508 (2021).
1088 59. R. Feleke, R. H. Reynolds, A. M. Smith, B. Tilley, S. A. G. Taliun, J. Hardy, P. M.
1089 Matthews, S. Gentleman, D. R. Owen, M. R. Johnson, P. K. Srivastava, M. Ryten, Cross-
1090 platform transcriptional profiling identifies common and distinct molecular
1091 pathologies in Lewy body diseases. *Acta Neuropathol. (Berl.)* **142**, 449–474 (2021).
1092 60. N. G. Skene, S. G. N. Grant, Identification of Vulnerable Cell Types in Major Brain
1093 Disorders Using Single Cell Transcriptomes and Expression Weighted Cell Type
1094 Enrichment. *Front. Neurosci.* **10** (2016).
1095 61. M. V. Sofroniew, Astrocyte reactivity: subtypes, states, and functions in CNS innate
1096 immunity. *Trends Immunol.* **41**, 758–770 (2020).
1097 62. J. Mertens, D. Reid, S. Lau, Y. Kim, F. H. Gage, Aging in a Dish: iPSC-Derived and
1098 Directly Induced Neurons for Studying Brain Aging and Age-Related
1099 Neurodegenerative Diseases. *Annu. Rev. Genet.* **52**, 271–293 (2018).
1100 63. C. Farina, F. Aloisi, E. Meinl, Astrocytes are active players in cerebral innate immunity.
1101 *Trends Immunol.* **28**, 138–145 (2007).
1102 64. J. L. Zamanian, L. Xu, L. C. Foo, N. Nouri, L. Zhou, R. G. Giffard, B. A. Barres, Genomic
1103 analysis of reactive astrogliosis. *J. Neurosci.* **32**, 6391–6410 (2012).
1104 65. A. Soung, R. S. Klein, Viral Encephalitis and Neurologic Diseases: Focus on Astrocytes.
1105 *Trends Mol. Med.* **24**, 950–962 (2018).
1106 66. H.-J. Lee, J.-E. Suk, C. Patrick, E.-J. Bae, J.-H. Cho, S. Rho, D. Hwang, E. Masliah, S.-J.
1107 Lee, Direct Transfer of α-Synuclein from Neuron to Astroglia Causes Inflammatory
1108 Responses in Synucleinopathies *. *J. Biol. Chem.* **285**, 9262–9272 (2010).
1109 67. F. Cavaliere, L. Cerf, B. Dehay, P. Ramos-Gonzalez, F. De Giorgi, M. Bourdenx, A.
1110 Bessede, J. A. Obeso, C. Matute, F. Ichas, E. Bezard, In vitro α-synuclein neurotoxicity
1111 and spreading among neurons and astrocytes using Lewy body extracts from
1112 Parkinson disease brains. *Neurobiol. Dis.* **103**, 101–112 (2017).

1113 68. A. Filippini, V. Mutti, G. Faustini, F. Longhena, I. Ramazzina, F. Rizzi, A. Kaganovich, D.
1114 A. Roosen, N. Landeck, M. Duffy, I. Tessari, F. Bono, C. Fiorentini, E. Greggio, L.
1115 Bubacco, A. Bellucci, M. Missale, M. R. Cookson, M. Gennarelli, I. Russo, Extracellular
1116 clusterin limits the uptake of α-synuclein fibrils by murine and human astrocytes. *Glia*
1117 **69**, 681–696 (2021).
1118 69. J. Rostami, S. Holmqvist, V. Lindström, J. Sigvardson, G. T. Westermark, M. Ingelsson,
1119 J. Bergström, L. Roybon, A. Erlandsson, Human Astrocytes Transfer Aggregated Alpha-
1120 Synuclein via Tunneling Nanotubes. *J. Neurosci.* **37**, 11835–11853 (2017).
1121 70. C. Kim, S. Kwon, M. Iba, B. Spencer, E. Rockenstein, M. Mante, A. Adame, S. J. Shin, J.
1122 A. Fields, R. A. Rissman, S.-J. Lee, E. Masliah, Effects of innate immune receptor
1123 stimulation on extracellular α-synuclein uptake and degradation by brain resident
1124 cells. *Exp. Mol. Med.* **53**, 281–290 (2021).
1125 71. D. Gussakovsky, S. A. McKenna, Alu RNA and their roles in human disease states. *RNA*
1126 *Biol.* **18**, 574–585 (2021).
1127 72. R. La Piana, C. Uggetti, I. Olivieri, D. Tonduti, U. Balottin, E. Fazzi, S. Orcesi, Bilateral
1128 striatal necrosis in two subjects with Aicardi-Goutières syndrome due to mutations in
1129 ADAR1 (AGS6). *Am. J. Med. Genet. A.* **164A**, 815–819 (2014).
1130 73. Q. Li, M. J. Gloudemans, J. M. Geisinger, B. Fan, F. Aguet, T. Sun, G. Ramaswami, Y. I.
1131 Li, J.-B. Ma, J. K. Pritchard, S. B. Montgomery, J. B. Li, RNA editing underlies genetic
1132 risk of common inflammatory diseases. *Nature* **608**, 569–577 (2022).
1133 74. K. S. Levine, H. L. Leonard, C. Blauwendraat, H. Iwaki, N. Johnson, S. Bandres-Ciga, L.
1134 Ferrucci, F. Faghri, A. B. Singleton, M. A. Nalls, Virus exposure and neurodegenerative
1135 disease risk across national biobanks. *Neuron* **111**, 1086-1093.e2 (2023).
1136 75. W. Hoyer, T. Antony, D. Cherny, G. Heim, T. M. Jovin, V. Subramaniam, Dependence
1137 of α-Synuclein Aggregate Morphology on Solution Conditions. *J. Mol. Biol.* **322**, 383–
1138 393 (2002).
1139 76. M. J. Devine, M. Ryten, P. Vodicka, A. J. Thomson, T. Burdon, H. Houlden, F. Cavaleri,
1140 M. Nagano, N. J. Drummond, J.-W. Taanman, A. H. Schapira, K. Gwinn, J. Hardy, P. A.
1141 Lewis, T. Kunath, Parkinson's disease induced pluripotent stem cells with triplication
1142 of the α-synuclein locus. *Nat. Commun.* **2**, 440 (2011).
1143 77. K. Gupta, R. Patani, P. Baxter, A. Serio, D. Story, T. Tsujita, J. D. Hayes, R. A. Pedersen,
1144 G. E. Hardingham, S. Chandran, Human embryonic stem cell derived astrocytes
1145 mediate non-cell-autonomous neuroprotection through endogenous and drug-
1146 induced mechanisms. *Cell Death Differ.* **19**, 779–787 (2012).
1147 78. N. Seto-Salvia, N. Esteras, R. de Silva, E. de Pablo-Fernandez, C. Arber, C. E. Toomey, J.
1148 M. Polke, H. R. Morris, J. D. Rohrer, R. Patani, S. Wray, T. T. Warner, Elevated 4R-
1149 tau in Astrocytes From Asymptomatic Carriers of the MAPT 10+16 Mutation. *Res. Sq.*,
1150 doi: 10.21203/rs.3.rs-117443/v1 (2020).
1151 79. Y. Shi, P. Kirwan, J. Smith, H. P. C. Robinson, F. J. Livesey, Human cerebral cortex
1152 development from pluripotent stem cells to functional excitatory synapses. *Nat.*
1153 *Neurosci.* **15**, 477–486 (2012).
1154 80. O. Kopach, N. Esteras, S. Wray, A. Y. Abramov, D. A. Rusakov, Genetically engineered
1155 MAPT 10+16 mutation causes pathophysiological excitability of human iPSC-derived
1156 neurons related to 4R tau-induced dementia. *Cell Death Dis.* **12**, 1–12 (2021).
1157 81. O. Kopach, N. Esteras, S. Wray, D. A. Rusakov, A. Y. Abramov, Maturation and
1158 phenotype of pathophysiological neuronal excitability of human cells in tau-related
1159 dementia. *J. Cell Sci.* **133**, jcs241687 (2020).

82. O. Kopach, Y. Dobropolska, P. Belan, N. Voitenko, Ca2+-Permeable AMPA Receptors Contribute to Changed Dorsal Horn Neuronal Firing and Inflammatory Pain. *Int. J. Mol. Sci.* **24**, 2341 (2023).
83. A. Butler, P. Hoffman, P. Smibert, E. Papalexi, R. Satija, Integrating single-cell transcriptomic data across different conditions, technologies, and species. *Nat. Biotechnol.* **36**, 411–420 (2018).
84. T. Stuart, A. Butler, P. Hoffman, C. Hafemeister, E. Papalexi, W. M. Mauck, Y. Hao, M. Stoeckius, P. Smibert, R. Satija, Comprehensive Integration of Single-Cell Data. *Cell* **177**, 1888-1902.e21 (2019).
85. L. Zappia, A. Oshlack, Clustering trees: a visualization for evaluating clusterings at multiple resolutions. *GigaScience* **7**, giy083 (2018).
86. S. Chen, Y. Zhou, Y. Chen, J. Gu, fastp: an ultra-fast all-in-one FASTQ preprocessor. *Bioinformatics* **34**, i884–i890 (2018).
87. A. Dobin, C. A. Davis, F. Schlesinger, J. Drenkow, C. Zaleski, S. Jha, P. Batut, M. Chaisson, T. R. Gingeras, STAR: ultrafast universal RNA-seq aligner. *Bioinformatics* **29**, 15–21 (2013).
88. A. D. Yates, P. Achuthan, W. Akanni, J. Allen, J. Allen, J. Alvarez-Jarreta, M. R. Amode, I. M. Armean, A. G. Azov, R. Bennett, J. Bhai, K. Billis, S. Boddu, J. C. Marugán, C. Cummins, C. Davidson, K. Dodiya, R. Fatima, A. Gall, C. G. Giron, L. Gil, T. Grego, L. Haggerty, E. Haskell, T. Hourlier, O. G. Izuogu, S. H. Janacek, T. Juettemann, M. Kay, I. Lavidas, T. Le, D. Lemos, J. G. Martinez, T. Maurel, M. McDowall, A. McMahon, S. Mohanan, B. Moore, M. Nuhn, D. N. Oheh, A. Parker, A. Parton, M. Patricio, M. P. Sakthivel, A. I. Abdul Salam, B. M. Schmitt, H. Schuilenburg, D. Sheppard, M. Sycheva, M. Szuba, K. Taylor, A. Thormann, G. Threadgold, A. Vullo, B. Walts, A. Winterbottom, A. Zadissa, M. Chakiachvili, B. Flint, A. Frankish, S. E. Hunt, G. IIsley, M. Kostadima, N. Langridge, J. E. Loveland, F. J. Martin, J. Morales, J. M. Mudge, M. Muffato, E. Perry, M. Ruffier, S. J. Trevanion, F. Cunningham, K. L. Howe, D. R. Zerbino, P. Flicek, Ensembl 2020. *Nucleic Acids Res.* **48**, D682–D688 (2020).
89. L. Wang, S. Wang, W. Li, RSeQC: quality control of RNA-seq experiments. *Bioinformatics* **28**, 2184–2185 (2012).
90. P. Ewels, M. Magnusson, S. Lundin, M. Käller, MultiQC: summarize analysis results for multiple tools and samples in a single report. *Bioinformatics* **32**, 3047–3048 (2016).
91. R. Patro, G. Duggal, M. I. Love, R. A. Irizarry, C. Kingsford, Salmon provides fast and bias-aware quantification of transcript expression. *Nat. Methods* **14**, 417–419 (2017).
92. C. Soneson, M. I. Love, M. D. Robinson, Differential analyses for RNA-seq: transcript-level estimates improve gene-level inferences. F1000Research 4:1521 [Preprint] (2016). https://doi.org/10.12688/f1000research.7563.2.
93. M. I. Love, W. Huber, S. Anders, Moderated estimation of fold change and dispersion for RNA-seq data with DESeq2. *Genome Biol.* **15**, 550 (2014).
94. Y. I. Li, D. A. Knowles, J. Humphrey, A. N. Barbeira, S. P. Dickinson, H. K. Im, J. K. Pritchard, Annotation-free quantification of RNA splicing using LeafCutter. *Nat. Genet.* **50**, 151–158 (2018).
95. H. M. Amemiya, A. Kundaje, A. P. Boyle, The ENCODE Blacklist: Identification of Problematic Regions of the Genome. *Sci. Rep.* **9**, 9354 (2019).
96. D. Zhang, R. H. Reynolds, S. Garcia-Ruiz, E. K. Gustavsson, S. Sethi, S. Aguti, I. A. Barbosa, J. J. Collier, H. Houlden, R. McFarland, F. Muntoni, M. Oláhová, J. Poulton, M. Simpson, R. D. S. Pitceathly, R. W. Taylor, H. Zhou, C. Deshpande, J. A. Botia, L.

1207 Collado-Torres, M. Ryten, Detection of pathogenic splicing events from RNA-
1208 sequencing data using dasper. bioRxiv [Preprint] (2021).
1209 https://doi.org/10.1101/2021.03.29.437534.
1210 97. clusterProfiler: an R Package for Comparing Biological Themes Among Gene Clusters |
1211 OMICS: A Journal of Integrative Biology.
1212 https://www.liebertpub.com/doi/full/10.1089/omi.2011.0118.
1213 98. The UniProt Consortium, UniProt: the Universal Protein Knowledgebase in 2023.
1214 *Nucleic Acids Res.* **51**, D523–D531 (2023).
1215 99. E. K. Gustavsson, D. Zhang, R. H. Reynolds, S. Garcia-Ruiz, M. Ryten, ggtranscript: an R
1216 package for the visualization and interpretation of transcript isoforms using ggplot2.
1217 *Bioinformatics* **38**, 3844–3846 (2022).
1218 100. M. Piechotta, E. Wyler, U. Ohler, M. Landthaler, C. Dieterich, JACUSA: site-specific
1219 identification of RNA editing events from replicate sequencing data. *BMC*
1220 *Bioinformatics* **18**, 7 (2017).
1221 101. M. Piechotta, I. S. Naarmann-de Vries, Q. Wang, J. Altmüller, C. Dieterich, RNA
1222 modification mapping with JACUSA2. *Genome Biol.* **23**, 115 (2022).
1223 102. O. Tange, GNU Parallel 20230722 ('Пригóжин'), Zenodo (2023);
1224 https://doi.org/10.5281/zenodo.8175685.
1225 103. P. Danecek, J. K. Bonfield, J. Liddle, J. Marshall, V. Ohan, M. O. Pollard, A. Whitwham,
1226 T. Keane, S. A. McCarthy, R. M. Davies, H. Li, Twelve years of SAMtools and BCFtools.
1227 *GigaScience* **10**, giab008 (2021).
1228 104. W. McLaren, L. Gil, S. E. Hunt, H. S. Riat, G. R. S. Ritchie, A. Thormann, P. Flicek, F.
1229 Cunningham, The Ensembl Variant Effect Predictor. *Genome Biol.* **17**, 122 (2016).
1230 105. D. Nishimura, RepeatMasker. *Biotech Softw. Internet Rep.* **1**, 36–39 (2000).
1231 106. R. Feleke, R. H. Reynolds, A. M. Smith, B. Tilley, S. A. G. Taliun, J. Hardy, P. M.
1232 Matthews, S. Gentleman, D. R. Owen, M. R. Johnson, P. K. Srivastava, M. Ryten, Cross-
1233 platform transcriptional profiling identifies common and distinct molecular
1234 pathologies in Lewy body diseases. *Acta Neuropathol. (Berl.)* **142**, 449–474 (2021).
1235 107. F. A. Wolf, P. Angerer, F. J. Theis, SCANPY: large-scale single-cell gene expression data
1236 analysis. *Genome Biol.* **19**, 15 (2018).

1237

1238 Acknowledgements

1239 We would like to thank the donors for their fibroblast and brain tissue donation. We would
1240 also like to thank the Francis Crick Institute Flow Cytometry, Advanced Light Microscopy,
1241 Advanced Sequencing, and Bioinformatics and Biostatistics STPs for their help and equipment
1242 in conducting and analysing the flow cytometry, fluorescence microscopy, and single-cell
1243 RNA-seq experiments. This research was funded in whole or in part by Aligning Science Across
1244 Parkinson's [ASAP-000509 and ASAP-000463] through the Michael J. Fox Foundation for
1245 Parkinson's Research (MJFF). For the purpose of open access, the author has applied a CC BY
1246 public copyright license to all Author Accepted Manuscripts arising from this submission. AZW

1247 was supported through the award of a Clinical Research Fellowship funded by the Wolfson
1248 Foundation and Eisai Ltd. MLC was supported by a National Research Foundation of Korea
1249 funded by the Korean government (RS-2023-00266872, RS-2024-00343012) and the Daekyo-
1250 KAIST Research Center for Cognitive Enhancement. The study was supported by Wellcome
1251 Collaborative Award to DR (Ref 223131/Z/21/Z) and OK was employed on that grant. SG was
1252 supported by Wellcome (100172/Z/12/2) and is currently an MRC Senior Clinical Fellow
1253 (MR/T008199/1). MRy was supported by the UK Medical Research Council (MRC) through her
1254 award of Tenure-track Clinician Scientist Fellowship (MR/N008324/1). This work was funded
1255 in part by a grant from MJFF (Project Title: Reacting to alpha-synuclein: how astrocytes cause
1256 neuronal loss in Parkinson's Disease; Grant ID: 18004).

1257 The Orchid IDs of the ASAP affiliated authors are - KD: 0000-0003-1266-419X; MLC: 0000-
1258 0001-9414-8214; AZW: 0000-0002-7747-6870; JRE: 0000-0003-2923-281X; PLG: 0000-0001-
1259 6636-5940; JL: 0000-0002-2642-3293; MGP: 0000-0003-0585-0971; SGR : 0000-0003-4913-
1260 5312; EKG: 0000-0003-0541-7537; CT: 0000-0002-5146-3326; RHR: 0000-0001-6470-7919;
1261 SS: 0000-0002-9781-6879; SG: 0000-0003-4395-2661; MRy: 0000-0001-9520-6957

1262 Author Contributions

1263 Conceptualization: MRy, SG, MLC, AZW, PLG, AG, DA, CB, JB

1264 Methodology: MRy, SG, MLC, KD, AZW, PLG, SR, NSS, GY, RP, EKG, OK, SS, JRE , DA, CB, JB,
1265 TW, BEC

1266 Investigation: AZW, KD, MLC, PLG, CT, OK, JRE, JL, DA, MRo, JS

1267 Validation: AZW, SG, KD, MLC, PLG, CT, EKG, OK, JRE, JL, DA, ZC

1268 Formal analysis: AZW, MRy, MLC, KD, PLG, MGP, OK, SS

1269 Visualization: SG, AZW, MLC, KD, PLG, OK, SS, JRE, DA, DAR, JS

1270 Supervision: MRy, SG, SAGT, CT, SR, DAK, RP, SS, DAR

1271 Software: AZW, MRy, KD, GY, RHR

1272 Data curation: AZW, MRy, KD, PLG, MGP, OK, SS, DA

1273 Writing—original draft: AZW, MRy, SG, KD, MLC, PLG, OK

Writing—review and editing: AZW, MRy, SG, KD, MLC, PLG, SAGT, NSS, RP, RHR, EKG, SS, JRE, DA, CB, ZC, TW

Resources: MRy, SG, PLG, CT, AG, NSS, DAK, RP, DAR, RHR, JL, SGR , MRo, ZC, TW, BEC

Funding acquisition: MRy, SG, DAK, DAR

Project administration: MRy, SG, DAK

Competing interests

Author RHR is currently employed by CoSyne Therapeutics (Lead Bioinformatician). All work performed for this publication was performed in her own time, and not as a part of her duties as an employee. The authors declare no other competing interests.

Data and code availability

The data that support the findings of this study are available at https://zenodo.org/records/10608268 and https://doi.org/10.5281/zenodo.14242993. Bulk-tissue and single-cell RNA-sequencing data can be accessed through the European Genome–phenome Archive (Study ID: EGAS50000000751). The RNA editing results are available at https://zenodo.org/records/10630845. Protocols used in this study can be found in the repository Protocols.io and the DOIs can be found in Supplementary Table 14.

Code used for the analyses of bulk-tissue and single-cell RNA-sequencing data is available at https://github.com/karishdsa/ipscAstrNeurCocul (https://doi.org/10.5281/zenodo.14024385). Code for the RNA editing analyses is available at https://github.com/aaronwagen/Astrocytes_editing (DOI: 10.5281/zenodo.14164792). All data needed to evaluate the conclusions in the paper are present in the paper and/or the Supplementary Materials.

Figures

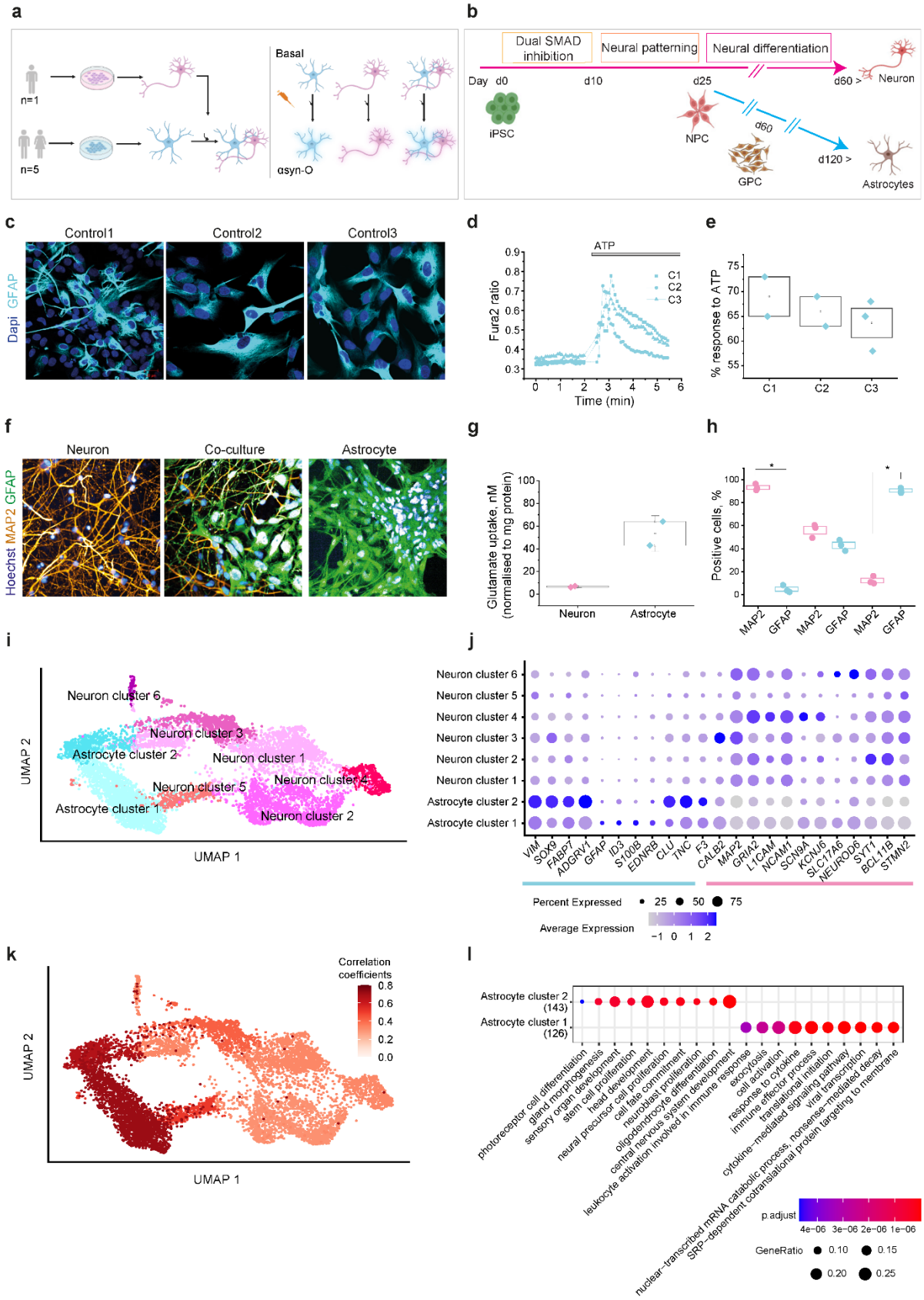

Figure 1. Schematic illustrations of experimental paradigm and the differentiation protocols.

(a) hiPSC-derived from five healthy individuals are differentiated into astrocytes (in-house lines: C1, C2, C3, commercial lines from ACS: C4, C5) and from one individual into neurons. (b) Differentiation of cortical region-specific astrocytes was performed, modifying established protocols(*77*, *78*). Neural precursor cells (NPCs) using an established protocol (Shi et al., 2012) were differentiated into either neurons and GPC (glial precursor cells) after 30 days from NPC, then further differentiated into mature astrocytes. (c) Immunocytochemistry images show that three lines of hiPSC-derived astrocytes express the astrocytic marker, GFAP. (d,e) There is a calcium response to APT in iPSC-derived astrocytes. Representative traces of calcium (d) and the percentage of cells (e) in response to ATP. (f) hiPSC-derived astrocyte enables uptake of glutamate (Glutamate Assay Kit, (ab83389/K629-100, Abcam). (g,h) Composition of hiPSC-derived neuron and astrocyte co-culture assessed using MAP2 (neuronal marker) and GFAP (astrocytic marker) immunocytochemistry together with representative images of a neuronal, astrocyte and co-culture (g) and the quantification (h). (i)UMAP plot showing the clustering of the integrated dataset using the cells from all the samples (basal and αsyn-O treated astrocytes, neurons, co-culture samples). (j) Dot plots showing the expression of the astrocyte and neuron marker genes in the clusters identified in the single-cell RNA-Seq data. (k) UMAP overlaid with the correlation coefficients, showing the correlation of the 2 astrocyte clusters with the astrocytes from Leng et al(*27*). (l) GO terms associated with the genes up-regulated in Astrocyte clusters 1 and 2. (a)&(b) were created with BioRender (https://biorender.com/)

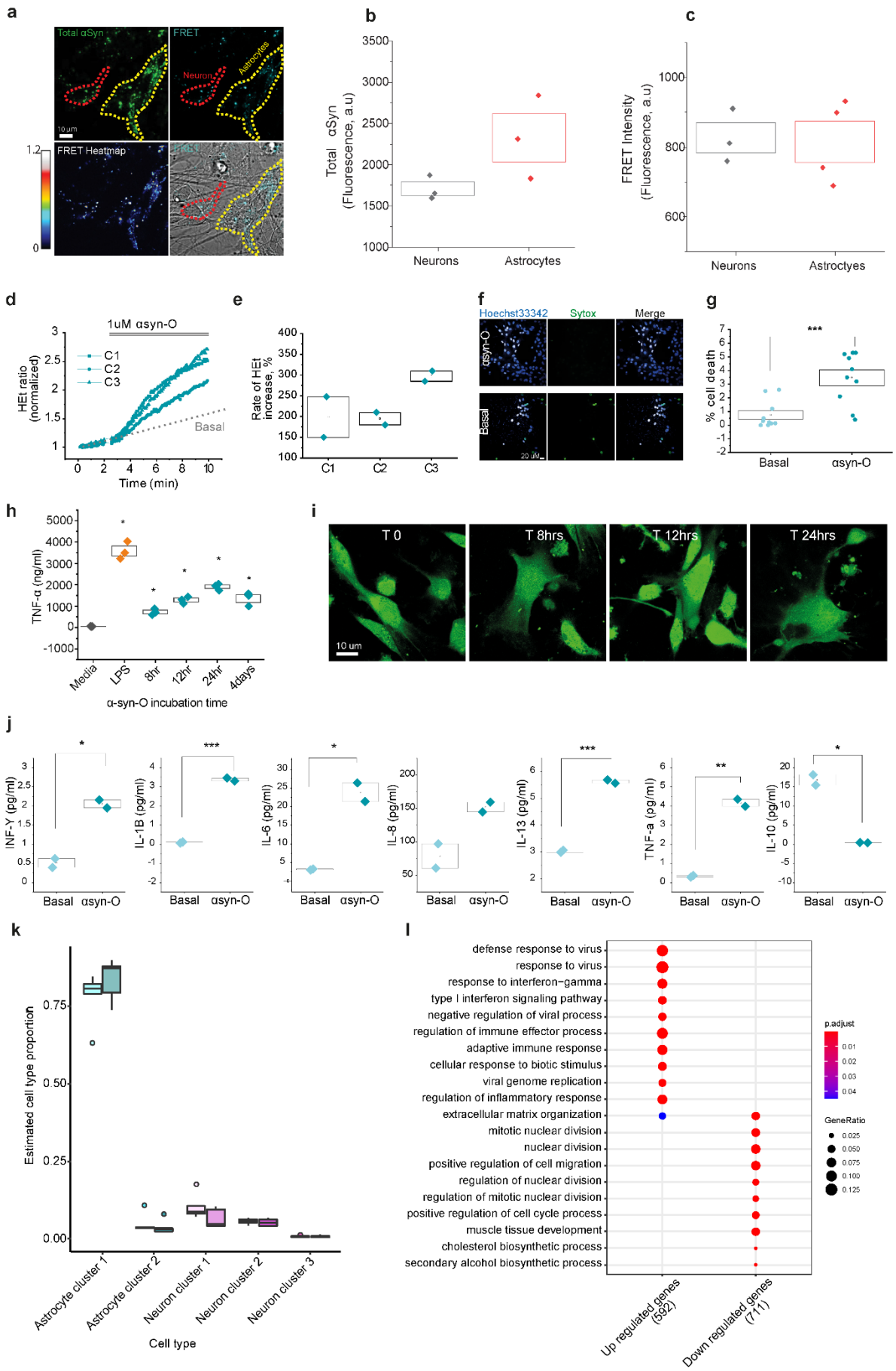
a
Total αSyn
FRET
Neuron
Astrocytes
10 um
FRET Heatmap
1.2
0
b
Total αSyn (Fluorescence, a.u)
Neurons
Astrocytes
c
FRET Intensity (Fluorescence, a.u)
Neurons
Astroctyes
d
1uM αsyn-O
HEt ratio (normalized)
C1
C2
C3
Basal
Time (min)
e
Rate of HEt increase, %
C1
C2
C3
f
Hoechst33342
Sytox
Merge
αsyn-O
Basal
20 uM
g
% cell death
***
Basal
αsyn-O
h
TNF-α (ng/ml)
Media
LPS
8hr
12hr
24hr
4days
α-syn-O incubation time
i
T 0
T 8hrs
T 12hrs
T 24hrs
10 um
j
INF-Y (pg/ml)
IL-1B (pg/ml)
IL-6 (pg/ml)
IL-8 (pg/ml)
IL-13 (pg/ml)
TNF-a (pg/ml)
IL-10 (pg/ml)
Basal
αsyn-O
k
Estimated cell type proportion
Astrocyte cluster 1
Astrocyte cluster 2
Neuron cluster 1
Neuron cluster 2
Neuron cluster 3
Cell type
l
defense response to virus
response to virus
response to interferon-gamma
type I interferon signaling pathway
negative regulation of viral process
regulation of immune effector process
adaptive immune response
cellular response to biotic stimulus
viral genome replication
regulation of inflammatory response
extracellular matrix organization
mitotic nuclear division
nuclear division
positive regulation of cell migration
regulation of nuclear division
regulation of mitotic nuclear division
positive regulation of cell cycle process
muscle tissue development
cholesterol biosynthetic process
secondary alcohol biosynthetic process
Up regulated genes (592)
Down regulated genes (711)
p.adjust
GeneRatio

1324 **Figure 2 Oligomer treatment of astrocytes induces an inflammatory state.**
1325

1326 (a) Uptake of monomeric species of labelled α-syn (A53T monomer) in astrocytes and neurons
1327 (yellow and red dotted lines respectively) was detected, and formation of oligomers inside
1328 cells confirmed using FRET. (b,c) No difference in the formation of oligomeric species
1329 observed despite higher uptake of total α-syn in astrocytes compared to neurons (n = 3
1330 independent inductions). (d,e) Application of αsyn-O induces overproduction of ROS. (f,g) Cell
1331 death induced by αsyn-O detected in astrocytes at low levels. (h) Cytokine release in αsyn-O
1332 treated astrocytes is time-dependent with TNF- α level highest after 24hr incubation with
1333 αsyn-O. (i) Morphological changes were traced using Fluo4 across the same time course as
1334 the cytokine release. (j) αsyn-O treated astrocytes induce an inflammatory state by releasing
1335 a range of cytokines (basal, αsyn-O treated for IL-13: 3.02 ± 0.04 pg/ml, 5.62 ± 0.05 pg/ml,
1336 IL-6: 3.11 ± 0.13 pg/ml, 23.8 ± 2.4 pg/ml, IL-8: 79.11 ±18.07 pg/ml, 152.01 ± 7.29 pg/ml, IL-1B:
1337 0.955 ± 0.03011, 3.38 ± 0.0772, INF-Y: 0.51 ± 0.11, 2.05 ± 0.1 pg/ml, TNF-α: 0.33 ± 0.0414,
1338 4.16 ± 0.187) (k) Cell type proportions (excluding cell types with proportions <1%) for each of
1339 the cell types in the bulk astrocyte samples, basal and αsyn-O treated, predicted by Scaden.
1340 (l) Top 10 GO terms associated with up and down-regulated differentially expressed genes at
1341 FDR < 5% and >= 2-fold change in expression in the astrocytes basally vs with αsyn-O
1342 treatment.

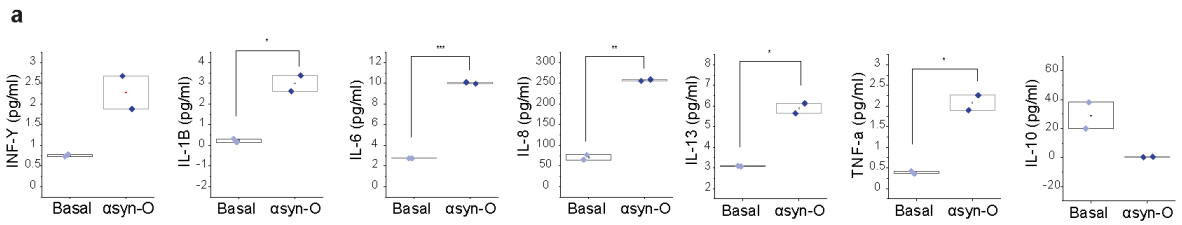
a
INF-Y (pg/ml)
IL-1B (pg/ml)
IL-6 (pg/ml)
IL-8 (pg/ml)
IL-13 (pg/ml)
TNF-a (pg/ml)
IL-10 (pg/ml)
Basal
αsyn-O

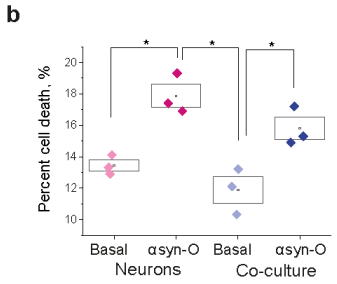
b
Percent cell death, %
Basal
αsyn-O
Neurons
Co-culture

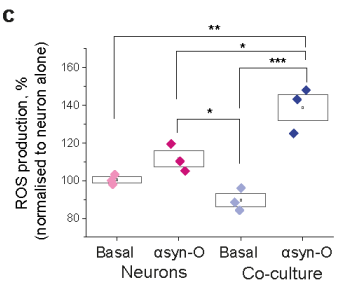
c
ROS production, %
(normalised to neuron alone)
Basal
αsyn-O
Neurons
Co-culture

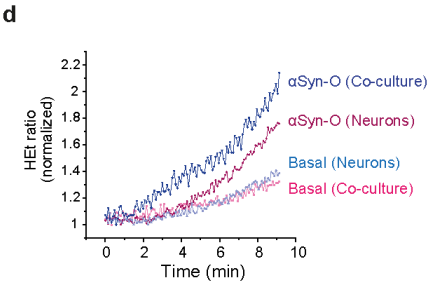
d
HEt ratio
(normalized)
αSyn-O (Co-culture)
αSyn-O (Neurons)
Basal (Neurons)
Basal (Co-culture)
Time (min)

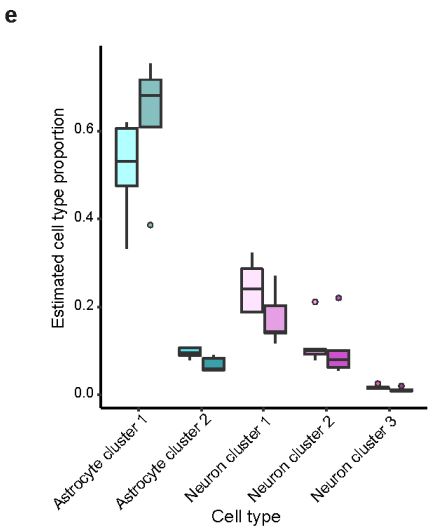
e
Estimated cell type proportion
Astrocyte cluster 1
Astrocyte cluster 2
Neuron cluster 1
Neuron cluster 2
Neuron cluster 3
Cell type

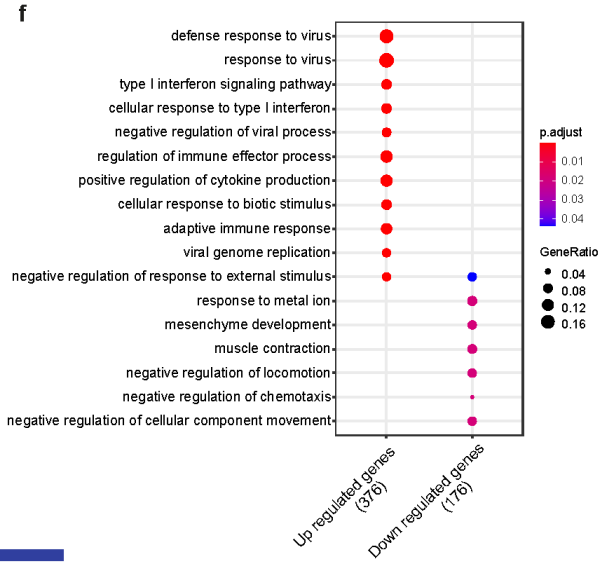
f
defense response to virus
response to virus
type I interferon signaling pathway
cellular response to type I interferon
negative regulation of viral process
regulation of immune effector process
positive regulation of cytokine production
cellular response to biotic stimulus
adaptive immune response
viral genome replication
negative regulation of response to external stimulus
response to metal ion
mesenchyme development
muscle contraction
negative regulation of locomotion
negative regulation of chemotaxis
negative regulation of cellular component movement
Up regulated genes (376)
Down regulated genes (176)
p.adjust
GeneRatio

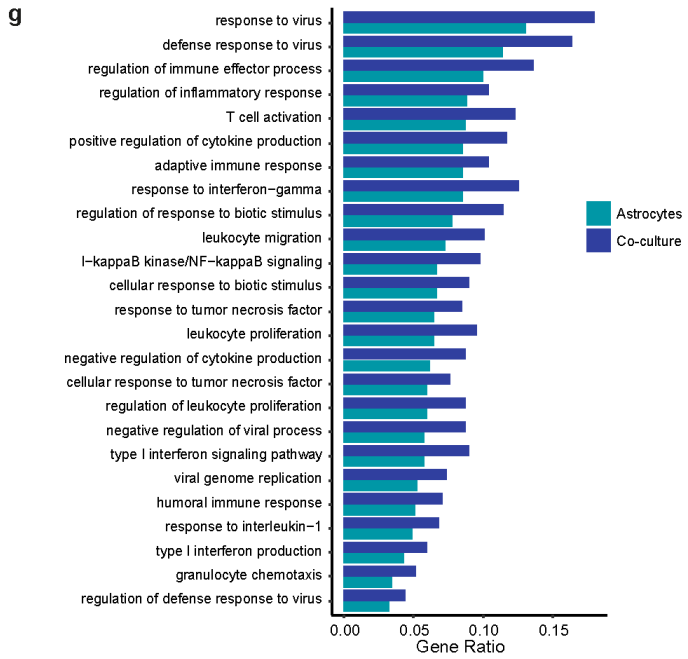
g
response to virus
defense response to virus
regulation of immune effector process
regulation of inflammatory response
T cell activation
positive regulation of cytokine production
adaptive immune response
response to interferon−gamma
regulation of response to biotic stimulus
leukocyte migration
I−kappaB kinase/NF−kappaB signaling
cellular response to biotic stimulus
response to tumor necrosis factor
leukocyte proliferation
negative regulation of cytokine production
cellular response to tumor necrosis factor
regulation of leukocyte proliferation
negative regulation of viral process
type I interferon signaling pathway
viral genome replication
humoral immune response
response to interleukin−1
type I interferon production
granulocyte chemotaxis
regulation of defense response to virus
Astrocytes
Co-culture
Gene Ratio

1343

Figure 3 Co-culture setting provides evidence of the astrocytes becoming more inflammatory.

(a) Effect of αsyn-O on cytokine release in the co-cultures (basal IL-13: 3.091 ± 0.0139 pg/ml, αsyn-O treated 5.88 ± 0.238 pg/ml, IL-6: basal 2.75 ± 0.00174 pg/ml, αsyn-O treated 10.026 ± 0.0593 pg/ml, IL-8: basal 71.09 ± 6.107 pg/ml, αsyn-O treated 257.2 ± 1.58 pg/ml, IL-1B: basal: 0.231 ± 0.0835 pg/ml, αsyn-O treated 2.99 ± 0.381 pg/ml, INF-Y: basal 0.392 ± 0.0329, αsyn-O treated 2.078 ± 0.180 pg/ml, TNF-α: basal 0.392 ± 0.0329, αsyn-O treated 2.078 ± 0.1801) (b,c,d) αsyn-O induces toxicity in neurons alone and in co-culture with astrocytes, and induces increased levels of ROS in neurons alone and in co-culture . (e) Plot showing the cell type proportions estimated by Scaden from the single cell data in the co-culture samples, basally (lighter shade) and with αsyn-O treatment (darker shade). There is a significant difference between the cell type proportions of astrocyte cluster 1 and 2 in the co-culture with αsyn-O treated compared to basal. (f) GO terms associated with the up- and down-regulated differentially expressed genes with at least >= 2-fold change in expression in the co-culture αsyn-O treated vs basal (g) Visualising gene ratios of the enrichments observed in the up-regulated differentially expressed genes of the astrocytes (cyan) compared to that of the co-culture (blue).

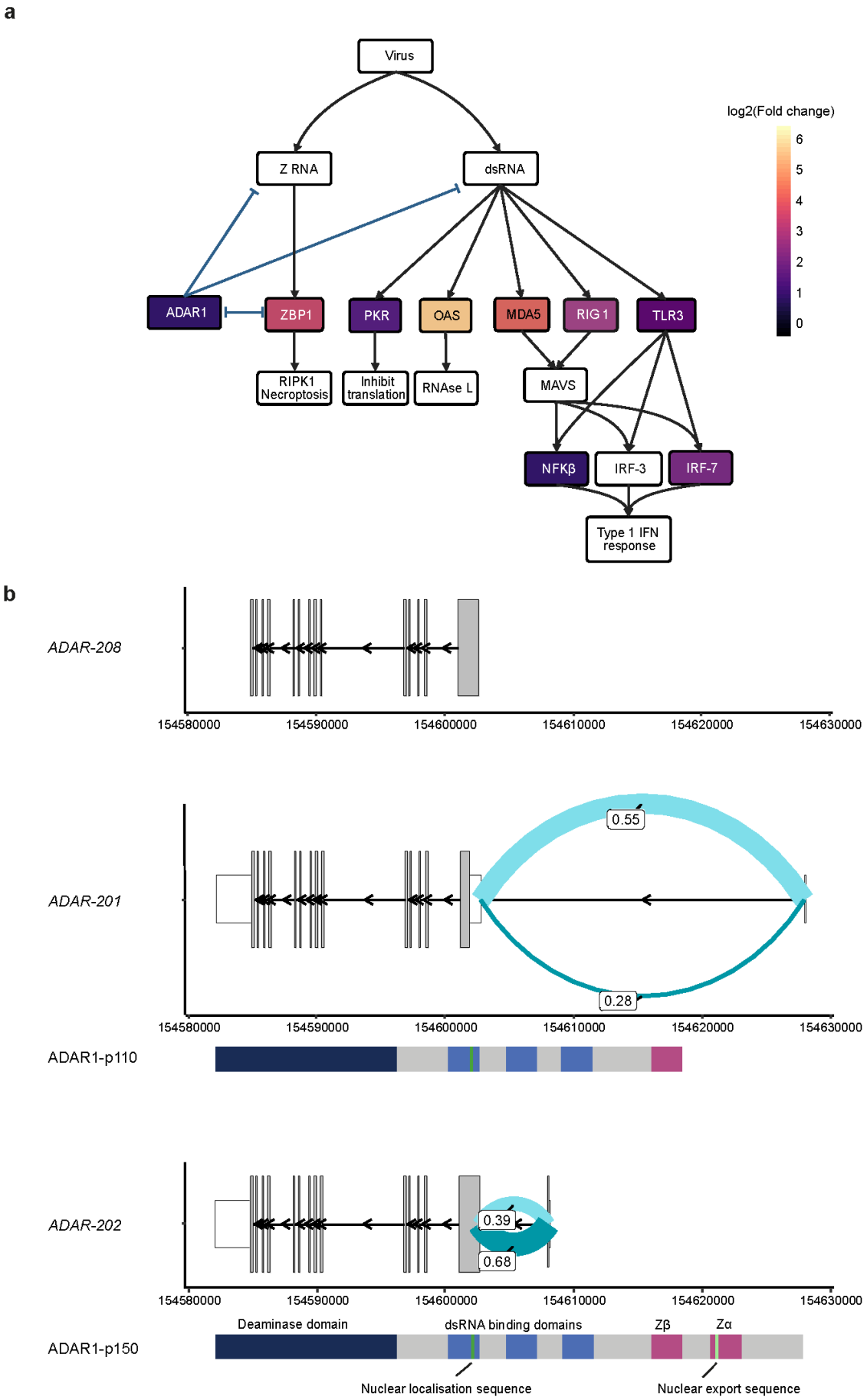
a
Virus
Z RNA
dsRNA
log2(Fold change)
6
5
4
3
2
1
0
ADAR1
ZBP1
PKR
OAS
MDA5
RIG 1
TLR3
RIPK1 Necroptosis
Inhibit translation
RNAse L
MAVS
NFKβ
IRF-3
IRF-7
Type 1 IFN response
b
ADAR-208
154580000
154590000
154600000
154610000
154620000
154630000
ADAR-201
0.55
0.28
ADAR1-p110
ADAR-202
0.39
0.68
ADAR1-p150
Deaminase domain
dsRNA binding domains
Zβ
Zα
Nuclear localisation sequence
Nuclear export sequence

1361

Figure 4 Type 1 IFN response leads to activation of *ADAR* (a) Model summarizing the role of *ADAR* in regulating the innate immune response to dsRNA with the $\log_2$(Fold change) of the genes that are significantly differentially expressed (at FDR < 5%) in the astrocytes on αsyn-O treatment. Model created with BioRender (https://biorender.com/) (b) Plot showing the significantly differentially spliced junctions in *ADAR* in the astrocytes on αsyn-O treatment, with the transcripts and protein isoforms. (Co-culture: **Supp figure 5a, b**).

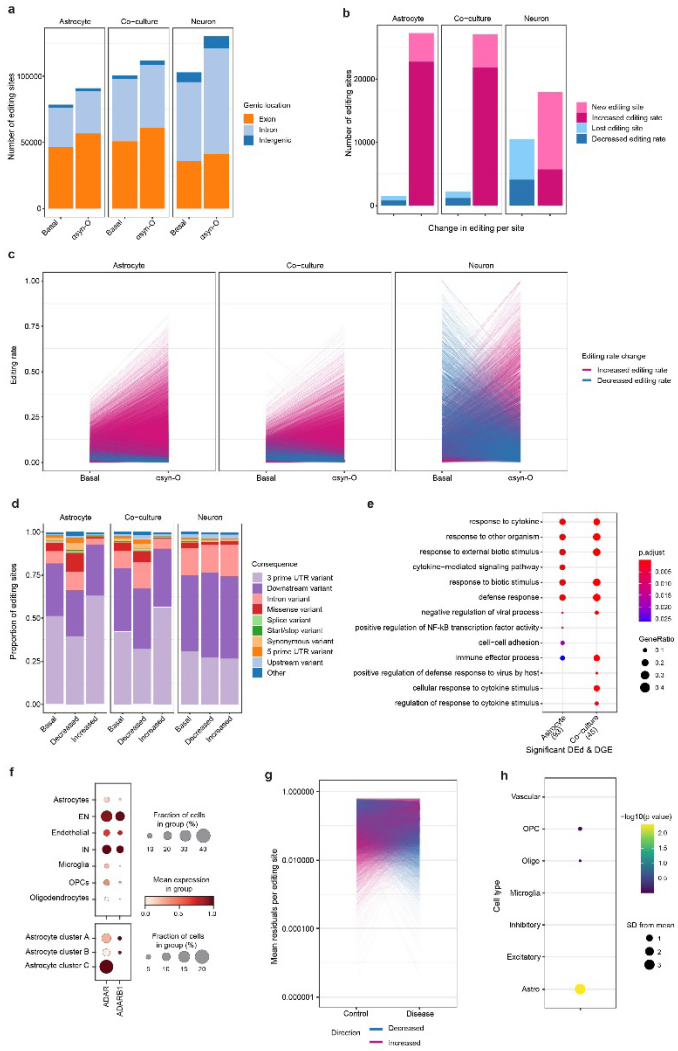

Figure 5 *ADAR* induced in A to I editing in astrocytes and co-cultures with αsyn-O treatment. (a) Number of editing sites in each sample, showing genomic locations (b) Number of differentially edited sites when comparing αsyn-O treated to samples basally in each culture. X-axis shows the decreased editing (blue, including lost) and increased editing (pink, including new). (c) Change in editing rate in basal vs αsyn-O treated samples in each culture. (d) Consequences of editing sites at baseline, and in differentially decreased or increased sites across cultures. (e) GO terms associated with the significantly differentially edited and differentially expressed (FDR < 5% and FC >=2) in the astrocytes and co-culture αsyn-O, treated vs basal. (f) Expression of *ADAR* and *ADARB1* in single nuclear post-mortem brain RNA. The top panel shows expression by cell-type, and the bottom shows expression within astrocytic clusters. Astrocyte cluster A is defined by expression of *ADGRV1* and *SLC1A2*; Astrocyte cluster B by *GFAP*, *S100B*, *AQP4* and Astrocyte cluster C by *VIM*, *SOX9* and *FOS*. (g) Mean residuals per editing site, after correction for covariates, in controls and diseased PD

post-mortem brain samples. (h) Expression weighted celltype enrichment analysis of genes with 50 greatest increase in mean editing rate.
Abbreviations: EN - excitatory neurons. IN - inhibitory neurons. OPC - oligodendrocyte progenitor cells.

Supplementary figures

1394

1395

1396

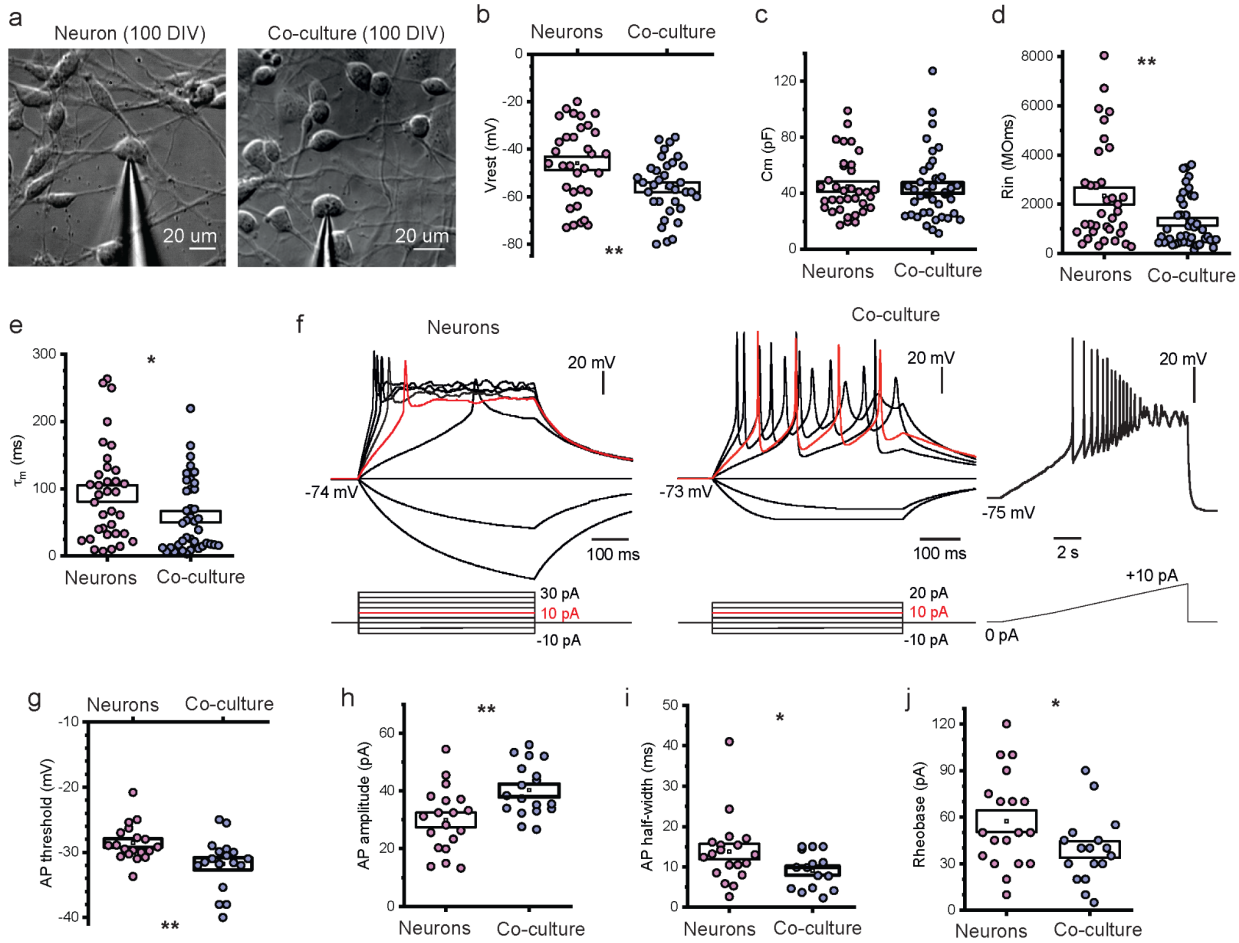

1397

1398

1399 **Supp figure 1**

1400

1401 (a) Transmitted light images of iPSC-derived cells in neuronal culture (left) and neuron-astrocytic co-culture
1402 (right) for whole-cell recordings made from individual neurons using patch pipettes. (b) Statistical summary of
1403 the resting membrane potential (Vrest) revealed more hyperpolarised Vrest of iPSC-derived cortical neurons in
1404 co-cultures than in the corresponding age-matched cultures. (c - e) Passive membrane properties of iPSC-derived
1405 cortical neurons showed similar cell capacity (Cm, Fig 3.c), but different membrane constant (τm, Fig 3.e) and
1406 input resistance (Rin, Fig 3.d) between neuronal cultures and co-cultures, indicating a difference in biophysical
1407 maturation of the neurons. All data are mean with s.e.m. *P < 0.05, **p < 0.01 (the two-tailed unpaired t-test).
1408 (f) Representative recordings of action potential (AP) firing in an iPSC-derived neuron evoked by a series of
1409 rectangular depolarising current pulses of increased intensity (indicated on the bottom) in cultures. (Bii) Example

1410 recordings of AP discharge generated by an iPSC-derived neuron evoked by square depolarising current pulses
1411 (left traces) or a slow-ramp current (indicated on the bottom) in co-cultures. Note a train of evoked APs in co-
1412 cultures.

1413 Analysis of individual APs across iPSC-derived cortical neurons revealed significant changes in the threshold (g),
1414 spike amplitude (h), half-width kinetic parameters (i), and rheobase (j).

1415

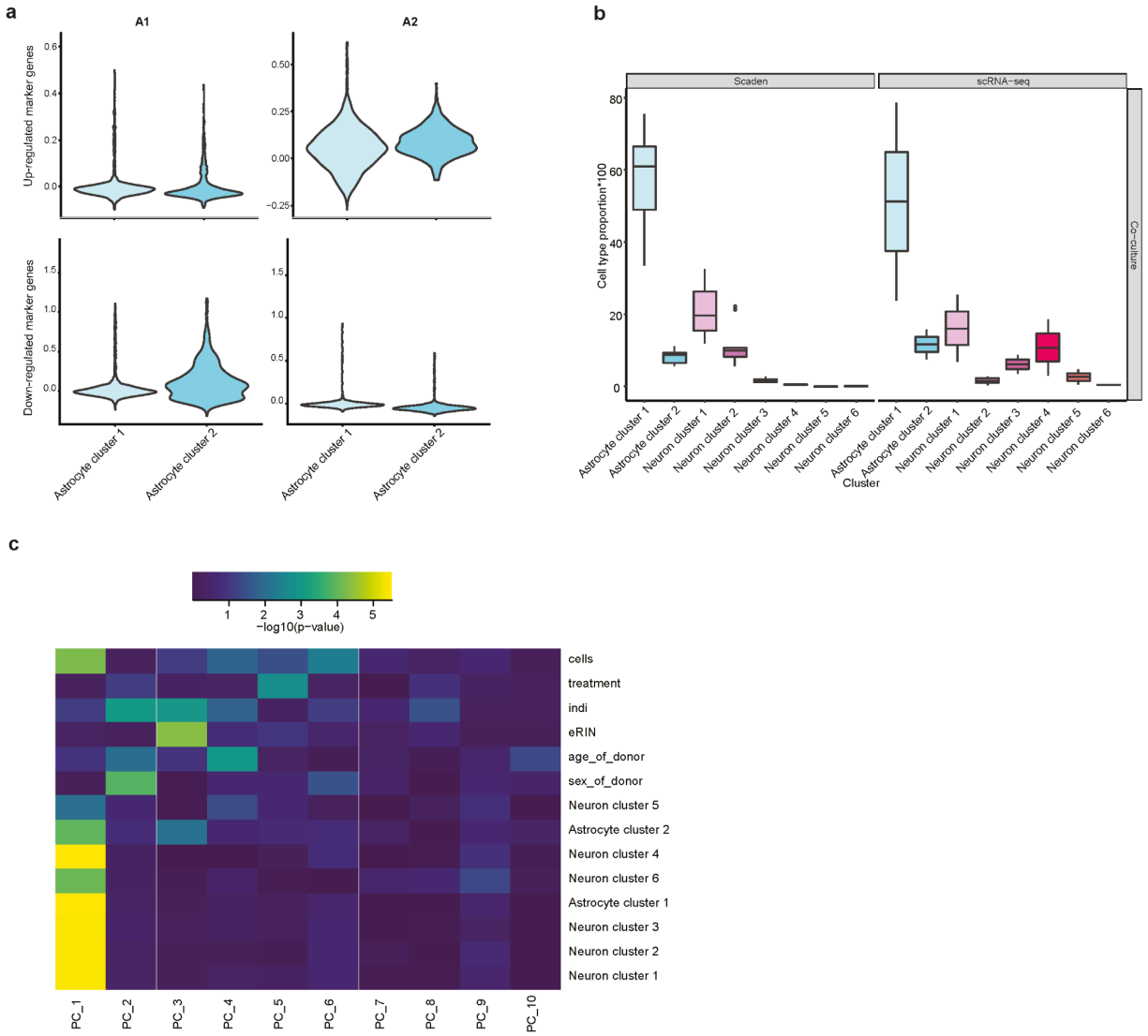

1416

1417 **Supp figure 2**

1418 (a) Visualising the module score of the published up and down regulated A1 and A2 marker genes in astrocyte
1419 clusters 1 and 2. The module score, generated per cell for a set of genes using the AddModuleScore() in Seurat,
1420 is the difference between the average expression of each gene set and random control genes, per cell. (b) Cell
1421 type proportions estimated by the single cell data vs that predicted by Scaden's deconvolution (c) Heatmap
1422 showing the correlation of the 1st 10 PCs with cell culture, treatment, individual, RIN , sex, age and the cell type
1423 proportions of the 8 cell types.

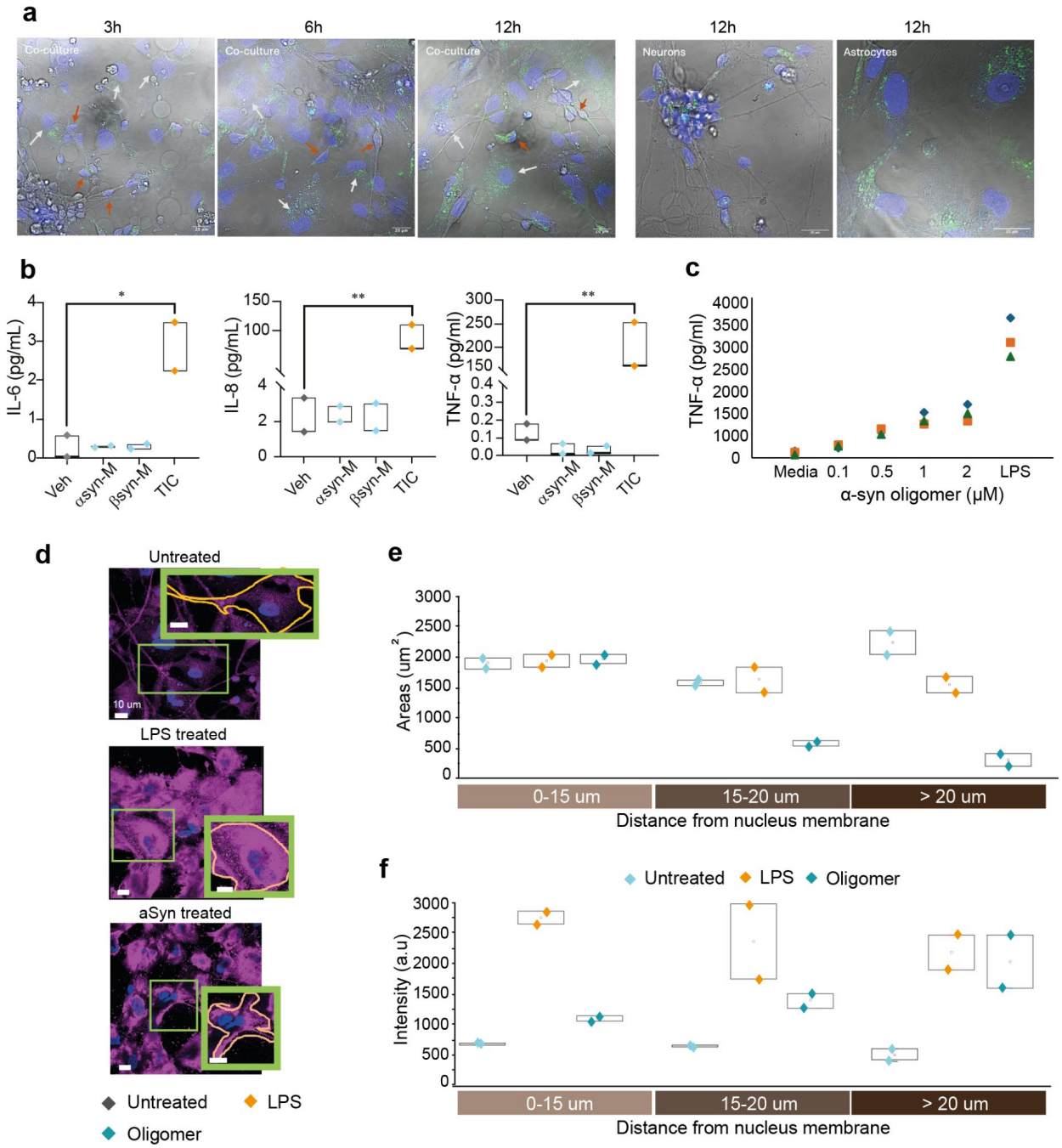

Supp figure 3

Astrocyte response to αsyn (a) Mono and co-cultures of astrocytes and neurons treated with fluorescent αsyn monomer 488 (500nM) at different time points (Monocultures treated for 12h; co-cultures treated for 3h, 6h and 12h). (b) Effect of different treatments on cytokine release in cortical astrocytes after a 24h incubation period (IL-6: Veh vs αsyn-M treated p>0.99, Veh vs βsyn-M p>0.99, Veh vs TIC p=0.0142; IL-8: Veh vs αsyn-M treated p>0.99, Veh vs βsyn -M p>0.99, Veh vs TIC p=0.0083; TNFα: Veh vs αsyn-M treated p>0.99, Veh vs βsyn-M p>0.99, Veh vs TIC p=0.0073). Veh, αsyn-M and βsyn-M treated at 1μM; TIC: TNFα: 30 ng/ml + IL1a: 3 ng/ml + C1q: 400 ng/ml. Each data point corresponds to a different donor line. (c) After iPSC-derived cortical astrocytes were treated overnight with αsyn-O or LPS, the media was refreshed and the cells were continued to be cultured

1434 for another 24 hours. The media was then collected to measure TNFα levels using an ELISA kit (R&D Systems).

1435 (d) Representative images of astrocytes immune labeled with GFAP demonstrating change in morphology upon
1436 stimulation by LPS or αsyn-O. Assessment of morphology by segmentation of astrocytes followed by (e) assessing
1437 GFAP pixel area, according to distance from nuclear membrane (measurement of polarity) and (f) intensity
1438 according to distance from nuclear membrane.[38,39]

1439

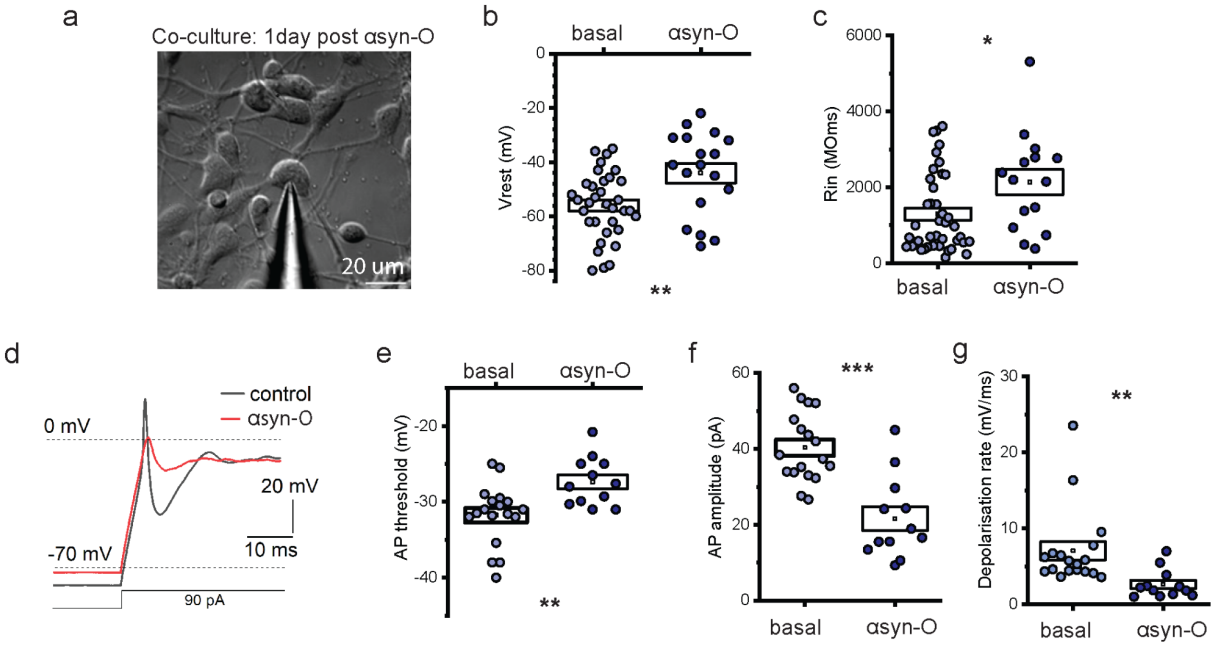

1440

1441 **Supp figure 4**

1442 (a) DIC image of neuron-astrocytic co-cultures for whole-cell recordings of iPSC-derived neurons 1 day after
1443 treatment with exogenous mutant α-syn. (b) Analyses of membrane properties revealed a depolarised Vrest in
1444 iPSC-derived neurons at 1-day post-treatment with the pathogenic protein. (c) Cortical neurons exhibited an
1445 increased Rin (Input resistance) following the treatment compared with the parameters in control (untreated)
1446 co-cultures. (d) Representative recordings of action potential spike in a control co-culture (black) and 1 day post-
1447 treatment with the pathogenic α-syn (red). Pathological α-syn impaired the shape and kinetics of individual
1448 action potential spikes, as measured for the parameters of threshold (e), amplitude (f) and depolarisation rates
1449 (g).

1450

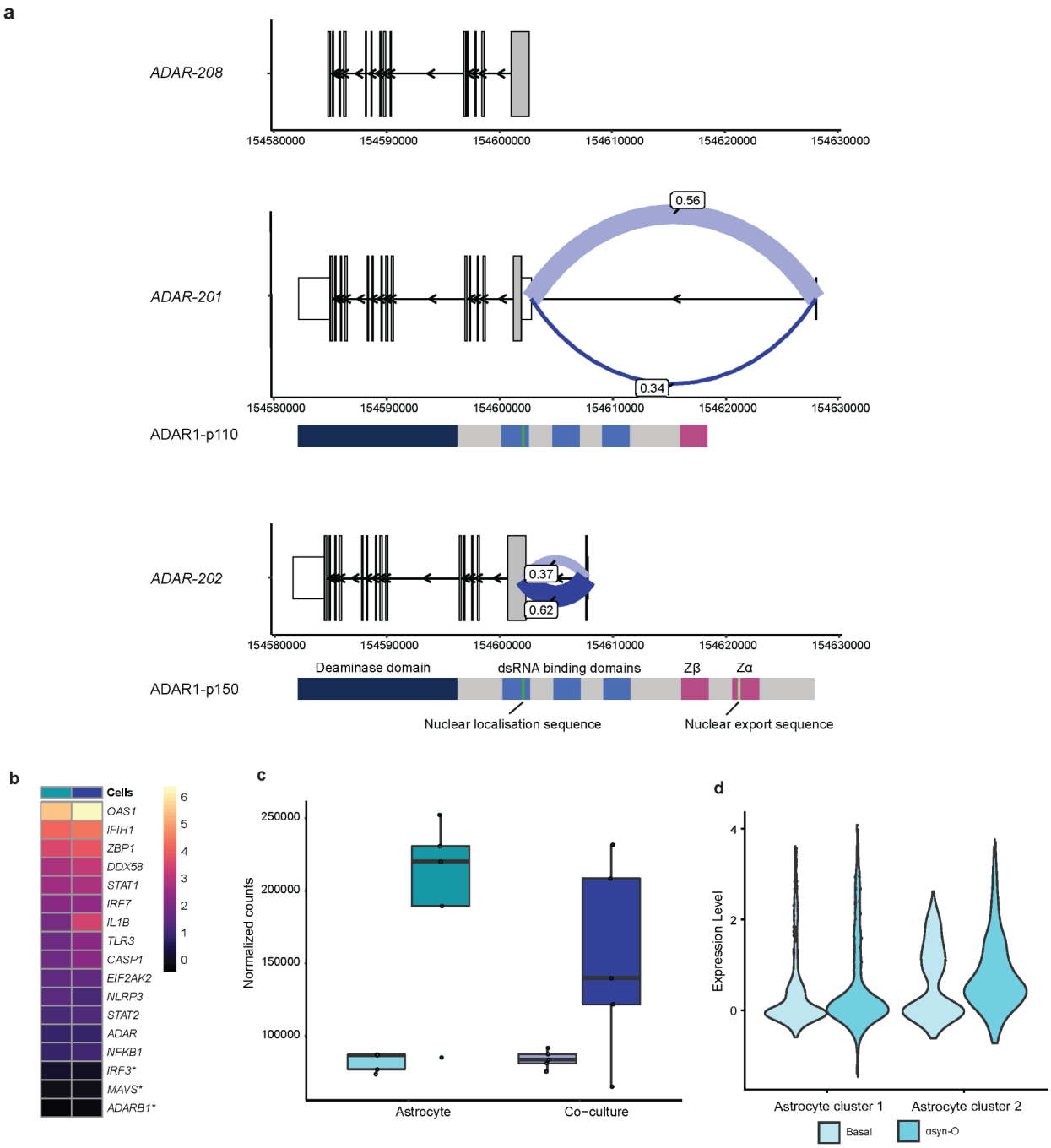

Supp figure 5

Differential gene expression and splicing of *ADAR* in co-culture on treatment with α-syn oligomers

(a) Splicing in *ADAR* showing alternate isoforms. Junctions are labelled with the junction usage (b) Heatmap showing the log_2FoldChange of the genes, in the innate immune response to dsRNA, (* not significantly differentially expressed at FDR < 5%) in the astrocytes and co-culture on αsyn-O treatment. (c) *ADAR* is differentially expressed in the astrocytes and co-culture on treatment with with α-syn oligomers (d) Expression

1461 of *ADAR* in the astrocyte cluster 1 and 2 in the single cell data

1462

1463

1464

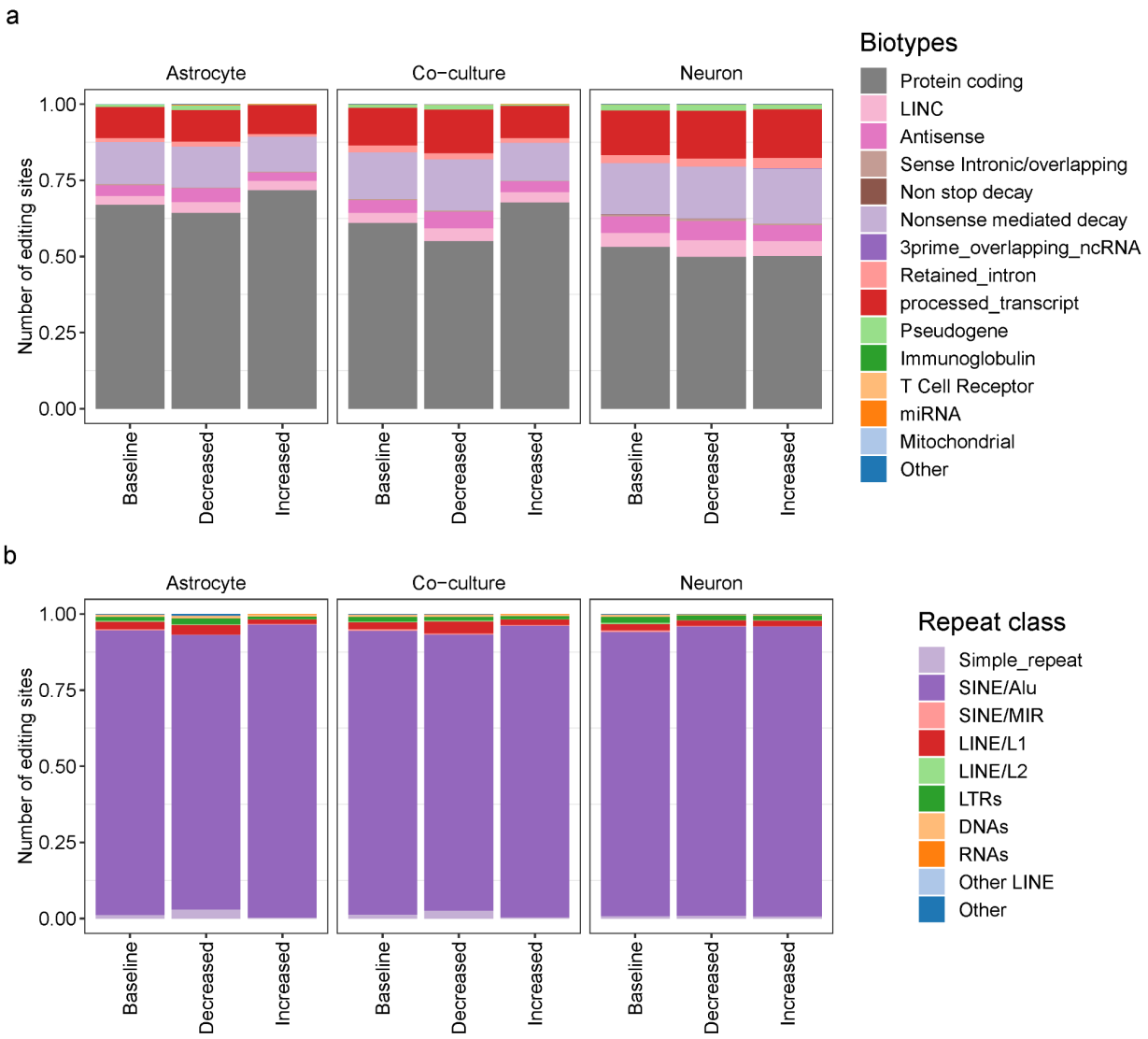

1465

1466 **Supp figure 6**

1467 Changes in proportion of editing sites with α-synO treatment in astrocytes, co-cultures and neurons showing a)
1468 biotypes annotated with Ensembl Variant Effect Predictor (v93.5). b) Proportion of repeat regions annotated
1469 with RepeatMasker.

1470

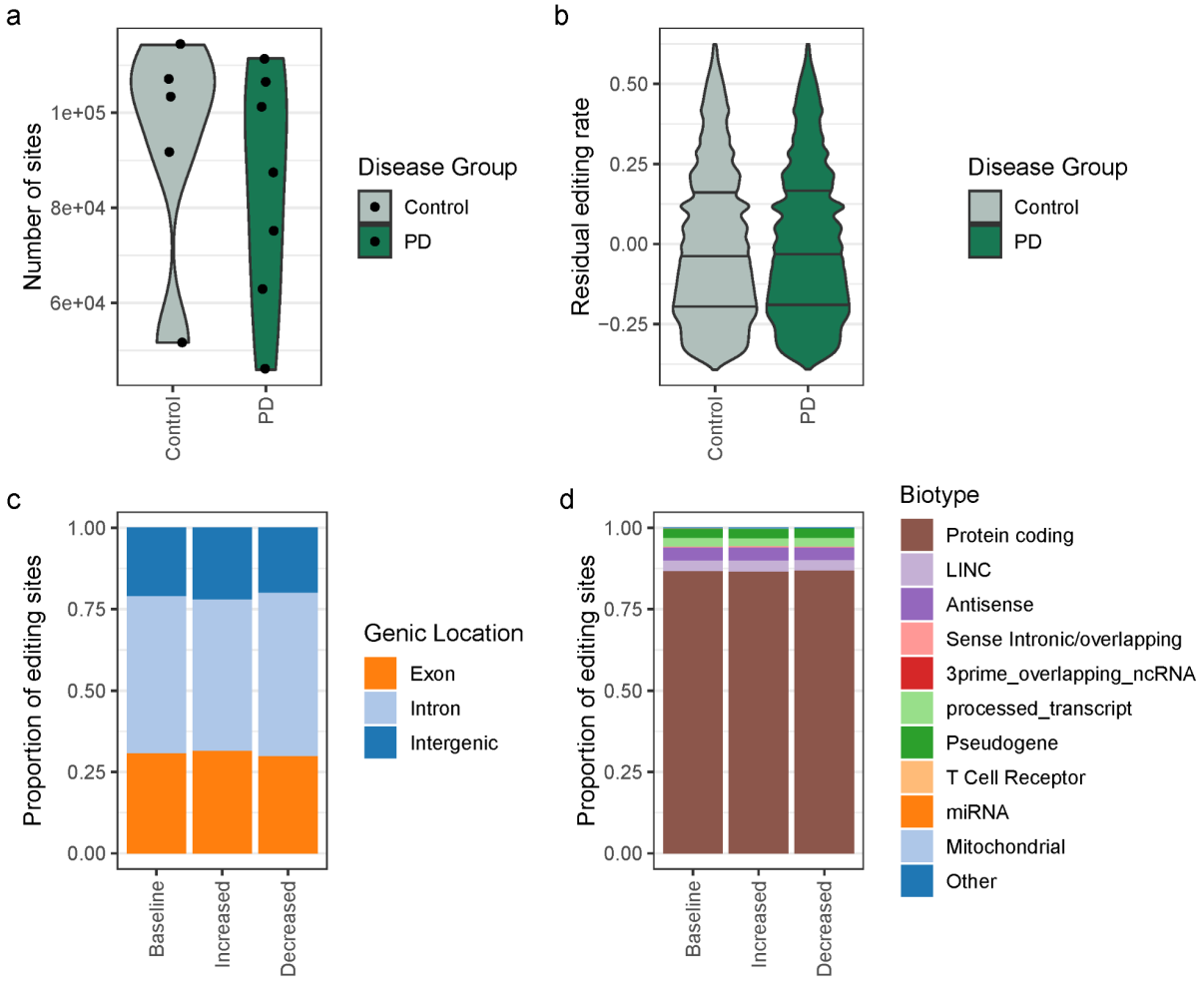

1471

1472 **Supp figure 7**

1473 A-to-I RNA editing in PD affected human brain. (a) The total number of sites per brain sample. (b) Residual editing
1474 rate after correction for covariates. The change in the proportion of sites that have increased or decreased
1475 editing, relative to baseline, in genic location (c), and biotype (d).

1476

1477 # Supplementary tables

1478 supplementary_tables.xls contains the Supplementary tables 1- 14

1479